

# Conservative data-driven finite element formulation

Adriana Kuliková<sup>a</sup>, Andrei G. Shvarts<sup>a,\*</sup>, Łukasz Kaczmarczyk<sup>a</sup>, Chris J. Pearce<sup>a</sup>

<sup>a</sup>*Glasgow Computational Engineering Centre (GCEC), James Watt School of Engineering, University of Glasgow, Glasgow, G12 8QQ, UK*

---

## Abstract

This paper presents a new data-driven finite element framework derived with mixed finite element formulation. The standard approach to diffusion problems requires the solution of the mathematical equations that describe both the conservation law and the constitutive relations, where the latter is traditionally obtained after fitting experimental data to simplified material models. To exploit all available information and avoid bias in the material model, we follow a data-driven approach. While the conservation laws and boundary conditions are satisfied by means of the finite element method, the experimental data is used directly in the numerical simulations, avoiding the need of fitting material model parameters. In order to satisfy the conservation law *a priori* in the strong sense, we introduce a mixed finite element formulation. This relaxes the regularity requirements on approximation spaces while enforcing continuity of the normal flux component across all of the inner boundaries. This weaker mixed formulation provides *a posteriori* error indicators tailored for this data-driven approach, enabling adaptive *hp*-refinement. The relaxed regularity of the approximation spaces makes it easier to observe how the variation in the datasets results in nonuniqueness of the solution, which can be quantified to predict the uncertainty of the results. The capabilities of the formulation are demonstrated on an example of the nonlinear heat transfer in nuclear graphite using synthetically generated material datasets.

*Keywords:* Data-driven mechanics, Diffusion problem, Finite element method, Weaker mixed formulation

---

## 1. Introduction

Classical computational approaches to engineering problems, such as solid and fluid mechanics, as well as diffusion and transport phenomena, require two components: conservation laws (complemented by appropriate boundary conditions) and constitutive behaviour of the materials. While conservation laws must be obeyed by all systems, any constitutive behaviour is an approximation of reality, often represented by material models obtained by fitting to the experimental data. Material models can vary from simple ones with one or two parameters (e.g. Darcy's flow, linear diffusion/heat flow, isotropic linear elasticity) to more complex ones (e.g. hyperelasticity, plasticity, unsaturated flow (Vogel et al., 2000), nonlinear heat transfer (Matsuo, 1980), among many others).

Fitting material models to experimental data allows for relatively fast and accurate solutions to boundary value problems using physics-based methods, depending on both the complexity of the model and the conformity of the fit. Examples of popular physics-based methods include the finite element method (FEM) (Zienkiewicz and Taylor, 2000), finite difference method (Smith, 1985), finite volume method (Versteeg, 2007), boundary

---

\*Corresponding author

*Email addresses:* [adriana.kulikova@glasgow.ac.uk](mailto:adriana.kulikova@glasgow.ac.uk) (Adriana Kuliková), [andrei.shvarts@glasgow.ac.uk](mailto:andrei.shvarts@glasgow.ac.uk) (Andrei G. Shvarts), [lukasz.kaczmarczyk@glasgow.ac.uk](mailto:lukasz.kaczmarczyk@glasgow.ac.uk) (Łukasz Kaczmarczyk), [chris.pearce@glasgow.ac.uk](mailto:chris.pearce@glasgow.ac.uk) (Chris J. Pearce)

element method (Katsikadelis, 2002), meshfree methods (Liu and Liu, 2003) and spectral methods (Boyd, 2001). Since the material models are often constructed using phenomenological laws, the existing models can be often reused for materials of similar types, allowing for extrapolation into states not included in the original experiments. For example, applying unsaturated flow models developed for soil (Vogel et al., 2000) to microfluidic flow in filter paper (Gerlero et al., 2022). However, certain materials may not directly fit any established model if the underlying phenomenon is unknown (Singh et al., 2022), exhibit changing properties over time due to usage conditions (Tzelepi et al., 2018; Jordan et al., 2018), or display inherent variance in their responses (Jones et al., 2019). Moreover, the fit of material models to actual material behaviour observed in experiments is often poorly understood, particularly regarding the conditions under which these constitutive relations apply (Edition and Bauld, 1986; Belytschko et al., 2014). Some materials may also exhibit stochastic behaviour, which is generally averaged out during model fitting, leading subsequent research to seek methods to reincorporate stochasticity into numerical analyses (Rao, 2013; Bensoussan, 1991).

Comparatively to the past, advances in data acquisition have enabled the collection of larger datasets from experimental studies on materials nowadays (Agarwal and Dhar, 2014; Baesens, 2014). The variability of this data, along with the different experimental setups and data collection methodologies, impacts how the data is incorporated into numerical simulations. Alternatives to traditional material models include machine learning (Bishop and Nasrabadi, 2006), neural networks (Bishop, 1995), and deep reinforcement learning (Arulkumaran et al., 2017), which can either identify material behaviour for future use or find solutions to entire problems. However, machine learning approaches which are used on their own may provide solutions that do not adhere to established physical laws (Pateras et al., 2023). Progress in this research area has led to the development of physics-informed machine learning (Pateras et al., 2023), constitutive artificial neural networks (Linka et al., 2021), and physics-informed neural networks (Raissi et al., 2019), bringing the solution back to obeying conservation laws (Grossmann et al., 2023). Nevertheless, machine learning approaches used on their own to obtain a complete numerical solution to mechanical or diffusion problems can be described as a “black box”, which can be used without the full understanding of the processes involved (Grossmann et al., 2023). This property, beneficial in some context, can be undesirable in others, where accuracy and control of errors is particularly important, e.g. structural integrity of safety-critical structures. To remove the “black box” element of the numerical analysis utilising material data, a new approach emerged named data-driven computational mechanics (Kirchdoerfer and Ortiz, 2016)

Data-driven computational mechanics provides an alternative to creating material models and allows the use of the data directly in numerical simulations while satisfying conservation laws by means of the finite element method. This method requires the dataset to define relationships between key variables that would typically be represented in a material model, e.g. stress and strain; heat flux and gradient of temperature; heat flux, temperature and its gradient; etc. These relationships are captured as points within a multidimensional dataset, which can be searched, and where each variable represents a dimension. As data-driven computational mechanics enables the use of material datasets directly instead of constitutive models, this allows the inherent imperfections of the material datasets to influence the results and, therefore, provides future means of quantifying uncertainty related to the material behaviour.

The data-driven approach was initially developed for elastic stress-strain problems and has, since its first introduction, been expanding (Kirchdoerfer and Ortiz, 2017; Ayensa-Jiménez et al., 2018). The applications now include diffusion (Nguyen et al., 2020), elasticity (Conti et al., 2018), nonlinear elasticity (Nguyen and Keip, 2018), inelasticity (Eggersmann et al., 2019), plasticity, and fracture (Carrara et al., 2020). Other research areas also include retrieving material datasets through data-driven identification (Stainier et al.,

2019; Leygue et al., 2017, 2018; Valdés-Alonzo et al., 2022), multiscale analyses using data-driven approaches in one or multiple scales (Mora-Macías et al., 2020; Karapiperis et al., 2021) and methods for completing incomplete datasets (Ayensa-Jiménez et al., 2019).

Since the original framework of the data-driven computational mechanics can be presented as a formulation with two (or more) independently approximated fields, e.g stress and displacement (Conti et al., 2018; Korzeniowski, 2022), heat flux and temperature (Nguyen et al., 2020; Kuliková et al., 2021), it can be classified as a multi-field or *mixed* formulation (Boffi et al., 2013). In case of the heat transfer, the original data-driven formulation uses  $\mathbf{L}^2(\Omega, \mathbb{R}^n)$  (Lebesgue) space for the flux and  $H^1(\Omega, \mathbb{R})$  (Sobolev) space for the temperature, where  $\mathbf{L}^2(\Omega, \mathbb{R}^n)$  is a space for vector functions with square integrable values and  $H^1(\Omega, \mathbb{R})$  is a space for scalar functions with square integrable values and derivatives. This is akin to the choice of spaces in the standard (single-field) finite element approach (Zienkiewicz and Taylor, 2000), and we will refer this formulation as “stronger” data-driven formulation.

However, more natural functional spaces can be chosen for each of the fields (Brezzi et al., 2008; Wakeni et al., 2022; Boffi et al., 2013; Arnold, 1990). The primary variable in heat diffusion, i.e. temperature, after integration by parts, can be approximated in  $L^2(\Omega)$  space, which allows for the temperature to be discontinuous across the elements. Although the exact solution for temperature is always in  $H^1$  space,  $L^2$  space better approximates sharp irregularities. This is particularly relevant for the data-driven method, where the field values taken from the dataset may differ significantly even for different integration points inside one element, in the case of missing or noisy dataset. The secondary variable is the heat flux, which is approximated in  $H(\text{div}; \Omega)$  space, which automatically enforces the continuity of the normal flux component across any inner boundaries. Furthermore, such choice of spaces leads to naturally emerging error indicators and estimators with little extra computational cost (Ainsworth, 2008; Braess and Verfürth, 1996; Carstensen, 1997). Error indicators can be utilised for adaptive refinements of mesh and/or finite element approximation order (Zander et al., 2022).

In this paper, we propose, for the first time, a data-driven formulation using the more natural functional spaces to the unknown fields discussed above. Following (Demkowicz, 2024), we call this formulation “weaker” DD formulation. The data-driven framework developed in this paper focuses on nonlinear heat transfer through porous media, such as graphite used in nuclear reactors (Matsuo, 1980) or fibrous and foamed insulating materials used in thermal insulation (Larkin and Churchill, 1959). When dealing with porous media, radiation through the pores might have a significant impact on the thermal conductivity relative to the temperature the body is experiencing (Larkin and Churchill, 1959). Therefore, the constitutive relationship for heat is expressed by Fourier’s/Fick’s law, where the dependence of thermal conductivity on temperature can introduce nonlinearity to the system.

In the proposed framework, the adaptive refinement is guided by the error indicators and improved by considering the proximity of the computed fields to the material dataset, ensuring only the elements whose refinement might impact the solution are refined. This approach minimises the computational effort required to reach a desired accuracy.

At the same time, using a material dataset instead of a material model in the finite element analysis introduces uncertainty related to the material dataset to the results. The material dataset can be sparse, not cover all the required material states, contain noise or outliers, which can impact the solution accuracy. In industrial applications, it is important to not only obtain the results of the analysis but also quantify the certainty of their results. The errors/uncertainty have two sources, the finite element approximation errors and the material dataset quality. Since the finite element approximation errors can be controlled by adaptive

refinement, these errors should be reduced first to ensure the material dataset quality is the main source of uncertainty.

If the material dataset contains noisy material datapoints, the solution of the data-driven approach is not unique and the result can vary depending on the initial field values when using the same material dataset (Kirchdoerfer and Ortiz, 2017), the solution can be perturbed and the analysis repeated to quantify the non-uniqueness that indicates the uncertainty in the results. This allows for the quantification of uncertainty in the results, akin to Markov chain Monte Carlo simulations, which obtain the standard deviation of the results. Since this requires repeating the simulation multiple times, and search through the material dataset happens at every integration point, the adaptive refinement is needed to reduce the number of integration points for a given accuracy, which allows for the uncertainty quantification to be performed in a reasonable time frame.

All of the numerical analysis in this work has been performed using specifically developed data-driven module (Kulikova, 2021) in an open-source finite element software MoFEM (Kaczmarczyk et al., 2020).

The following section introduces the notation for the diffusion problem used throughout this work, forms of material dataset and its connection to the finite element formulation. Section 3 contains the derivation of “stronger” (original) and “weaker” data-driven finite element formulations and discussion of the differences between them. The verification of both formulations using a problem with a known exact solution is presented in section 4. Section 5 leverages the functional spaces used by the conservative “weaker” DD formulation to adapt the finite element error indicators and additionally introduces new data-driven error indicators, which are used together to form an adaptive *hp*-refinement strategy. A 2D model of nuclear graphite brick is used as a second numerical example which introduces more complexities and is used as full verification for the developed framework in section 6. The brick example continues to be used in section 7 where the non-uniqueness of the solution is quantified using Markov chain Monte-Carlo analysis to make prediction of the uncertainty of the result.

## 2. Data-driven approach for heat transfer in porous materials

This paper focuses on developing a novel, “weaker” data-driven approach for heat transport problems. However, the developed approach can be applied to any scalar transport problem or be extended to vector problems, e.g. elasticity (Kirchdoerfer and Ortiz, 2016), or coupled problems, e.g. thermo-elasticity with either or both parts utilising the data-driven formulation.

The conservation of energy for the heat transport problem reads:

$$\nabla \cdot \mathbf{q} = s \quad \text{in } \Omega, \quad (1)$$

where  $\mathbf{q}$  is the heat flux and  $s$  is the source in the domain  $\Omega$ . The boundary conditions are assumed to be:

$$\begin{cases} \mathbf{q} \cdot \mathbf{n} = \bar{q} & \text{on } \Gamma_q \\ T = \bar{T} & \text{on } \Gamma_T, \end{cases} \quad (2a)$$

$$(2b)$$

where  $\bar{q}$  is the normal flux,  $T$  is temperature and  $\bar{T}$  is its value defined on the corresponding part of the boundary  $\Gamma$ , see Figure 1 and Table 1.

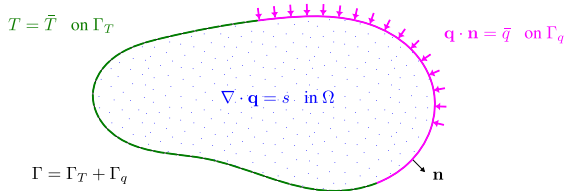


Figure 1: A sketch visualising the domain where the conservation of energy is fulfilled and the parts of the boundary where the Dirichlet and Neumann boundary conditions are applied.

BC type	Field on which the condition is applied	Boundary
Dirichlet	Primary variable: temperature $T$	$\Gamma_T$
Neumann	Secondary variable: heat flux $\mathbf{q}$	$\Gamma_q$

Table 1: Types of boundary conditions for boundary value problems.

To be able to solve a heat diffusion boundary value problem (1)-(2), in the standard FE approach, the flux  $\mathbf{q}$  is defined with the help of a phenomenological constitutive equation, i.e. Fourier’s law:  $\mathbf{q} = -k\nabla T$ . However, thermal conductivity  $k$  can introduce nonlinearity to the system by the dependence on the unknown temperature  $T$ , i.e.  $k = k(T)$ . Additionally, the thermal conductivity can be dependent on the spatial heterogeneity, such as the porosity of the material, which may evolve in time. The resulting constitutive relation could be highly nonlinear and depend on a set of empirical parameters (Lienhard and Lienhard, 2020).

On the contrary, in this paper, following (Kirchdoerfer and Ortiz, 2016), we assume no constitutive equation, while the necessary relationship between the heat flux  $\mathbf{q}$  and the gradient of temperature  $\nabla T$  is introduced through a material dataset. To replace the constitutive equation, the dataset dimensions need to contain the temperature gradient  $\mathbf{g}^*$  and the heat flux  $\mathbf{q}^*$ . The data-driven approach consists of two main parts:

1. Searching through a material dataset  $\mathcal{D}$  to find a subset of the closest material points to the current solution fields.
2. Solving the finite element problem with the subset of the material dataset.

To be able to visualise the material dataset, and hence the search through it, we begin with an introduction of material datasets and their handling, and explain the connection to the finite element formulation afterwards.

### 2.1. Material dataset creation

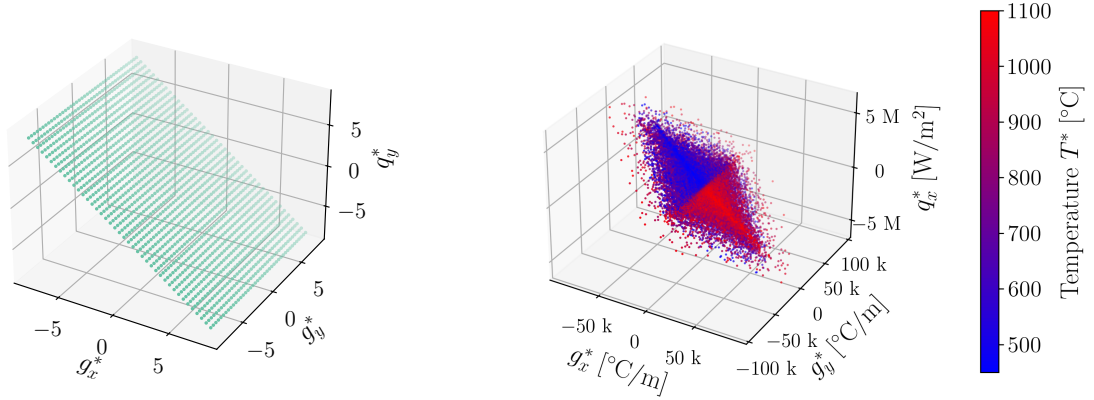
For this paper, all of the material datasets are generated for a two dimensional problem. Any material points originating from the dataset will be denoted as  $(\cdot)^*$ , e.g.  $\mathbf{g}^*$  represents the temperature gradient values from the material dataset.

For verification purposes, the first kind of material dataset is created with a constant thermal conductivity  $k = 1$  in a grid structure, see Figure 2(a). The data is generated for the gradients of temperature in  $x$  and  $y$  directions for a number of datapoints with equal spacing in ranges  $[-K, K]$  and  $[-K, K]$ , respectively. The heat flux is then computed as  $\mathbf{q}^* = -k\mathbf{g}^*$ , where  $k = 1$  is the thermal conductivity. This dataset will be referred to as *regular* in the following sections, and for the 2D domain, it is a 4D material dataset, each point of which can be denoted as  $\{g_x^*, g_y^*, q_x^*, q_y^*\}_{4D}$ .

The second material dataset creation method utilises artificial experiments with a nonlinear thermal conductivity of graphite based on the following empirical equation (McEligot et al., 2016):

$$k(T) = 134 - 0.1047T + 3.719 * 10^{-5}T^2, \quad (3)$$

where the thermal conductivity  $k$  is in  $W/mK$  and temperature  $T$  is in  $^\circ C$ . The visualisation of the thermal conductivity dependance on temperature, atrificial experiment setup and resulting dataset are shown in



(a) 4D material dataset generated at regular intervals with a linear constitutive law:  $k = 1$ . (b) 5D material dataset generated through artificial experiments with a nonlinear constitutive law.

Figure 2: Example material datasets with  $\mathbf{q}^* = -k\mathbf{g}^*$ , where  $k$  is the thermal conductivity. The dataset creation is explained in Appendix A.

subsection Appendix A.2. Varying the temperature of the inside and outside boundary,  $T_{\text{in}}$  and  $T_{\text{out}}$ , the temperature gradient and heat flux are computed using the standard finite element method and the values are saved in the material dataset for each integration point in the domain, see Figure 2(b). The material dataset contains five dimensions for a 2D domain, i.e. each datapoint is represented as  $\{T^*, g_x^*, g_y^*, q_x^*, q_y^*\}_{5D}$ , and will be referred to as *artexp* dataset in the following sections. More details about the creation of the material datasets in this paper can be found in Appendix A.

It is important to note that additional dimensions can be included according to an assumed dependency and the availability of the material data.

## 2.2. Searching through the material dataset

Assuming a 5D material dataset  $\mathcal{D}_{5D} = \{T^*, g_x^*, g_y^*, q_x^*, q_y^*\}$ , the search through the dataset can be performed by minimising the distance of the unknown fields to the dataset. Starting with random or zero initial values for the unknown fields, the distance between the material dataset and the unknown field values can be minimised. For every point  $(x, y)$  in the domain  $\Omega$ , we can define the distance of the values of the temperature  $T$ , temperature gradient  $\nabla T$  and heat flux  $\mathbf{q}$  to the dataset  $\mathcal{D}_{5D}$  as follows:

$$\text{dist}(\{T, \nabla T, \mathbf{q}\}, \mathcal{D}_{5D}) = \min_{\{T^*, \mathbf{g}^*, \mathbf{q}^*\} \in \mathcal{D}_{5D}} \sqrt{S_T (T - T^*)^2 + S_g (\nabla T - \mathbf{g}^*)^2 + S_q (\mathbf{q} - \mathbf{q}^*)^2}, \quad (4)$$

where  $S_T$ ,  $S_g$  and  $S_q$  are stabilisation/scaling parameters that depend on a numerical scheme and, in our case, make the distance between dataset points unitless. The material dataset and the dataset search can include more or less dimensions than the five presented above, e.g. the temperature  $T$  can be omitted as is the case with the *regular* dataset shown in Figure 2(a). However, the temperature gradient  $\mathbf{g}$  and heat flux  $\mathbf{q}$  always need to be included in the material dataset and search.

The examples in this paper use R-tree index structure for spatial searching (Guttman, 1984). However, the minimisation Eq. (4) can be replaced by other algorithms such as approximate nearest-neighbour,  $k$ -means tree, geometric near-neighbour access tree or algorithms based on Mahalanobis distance (Eggersmann et al., 2021; Bahmani and Sun, 2021; Ayensa-Jiménez et al., 2018).

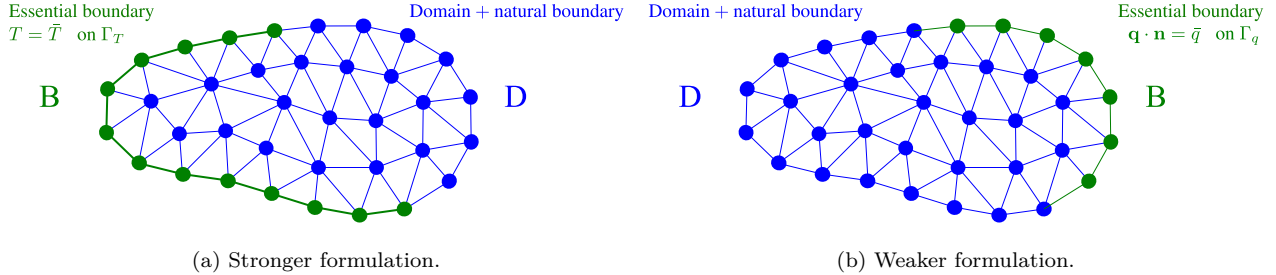


Figure 3: Discretisation of the domain  $\Omega$  with the essential boundary  $\Gamma_T$  for the standard formulation (a) and the essential boundary  $\Gamma_q$  for the mixed formulation (b) of the heat diffusion problem, cf. Fig. 1. The essential boundary is represented by the degrees of freedom  $B$  and the rest of the domain by the degrees of freedom  $D$ .

### 2.3. Connection to finite element formulation

The dataset search (4) is used to find the closest material points to the current solution fields at every integration point in the domain. A functional representing the integrated distance of the unknown fields  $\nabla T$  and  $\mathbf{q}$  to the dataset  $\mathcal{D}$  can be defined as follows:

$$J(\nabla T, \mathbf{q}) = \int_{\Omega} S_g (\nabla T - \mathbf{g}^*)^2 d\Omega + \int_{\Omega} S_q (\mathbf{q} - \mathbf{q}^*)^2 d\Omega, \quad (5)$$

where the data point  $\{T^*, \mathbf{g}^*, \mathbf{q}^*\}_{5D}$  or  $\{\mathbf{g}^*, \mathbf{q}^*\}_{4D}$  is found as a minimiser of (4).

The integrated distance functional  $J(\nabla T, \mathbf{q})$  (5) does not contain temperature variables  $T$  and  $T^*$  because the relationship between the gradient of temperature and heat flux is dictated by Fourier's law, a fundamental principle in thermodynamics. Fourier's law dictates that heat flows from regions of higher temperature to regions of lower temperature, connecting the heat flux and temperature gradient only. Consequently, temperature  $T$  should solely be used to identify the material state of heat flux  $\mathbf{q}$  and temperature gradient  $\nabla T$  through  $\mathbf{q}^*$  and  $\mathbf{g}^*$ .

## 3. Data-driven finite element formulations

The following section explores two data-driven finite element formulations for solving heat transfer problems: the original one (stronger) and the one proposed in this paper (weaker). Both start from the same set of equations consisting of the conservation law (1), boundary conditions (2) and the integrated distance functional (5).

The key difference between the stronger and weaker formulations lies in the function spaces used for approximation of the unknown functions, see Table 2. While the stronger formulation utilises the Sobolev space  $H^1(\Omega)$  for the temperature and the Lebesgue space  $\mathbf{L}^2(\Omega)$  for the flux, the weaker formulation uses the Lebesgue space  $L^2(\Omega)$  for the temperature and the Sobolev space  $H(\text{div}; \Omega)$  for the flux. The weaker formulation is more natural for the heat transfer problem as it enforces continuity of the normal flux component across inner boundaries. Moreover, in the weaker formulation, the Dirichlet and Neumann boundary conditions are enforced as natural and essential, respectively, which is the opposite of the stronger formulation and the standard FEM, see Figure 3.

Further comparisons between the stronger and weaker DD formulations are given after the derivations of the two formulations in the following subsections.

Field	Rank	Function space	
		Stronger DD	Weaker DD
Temperature	Scalar	$T \in H^1(\Omega) : T = \bar{T} \text{ on } \Gamma_T$	$T \in L^2(\Omega)$
Temperature gradient	Vector	Not used	$\mathbf{g} \in \mathbf{L}^2(\Omega)$
Heat flux	Vector	$\mathbf{q} \in \mathbf{L}^2(\Omega)$	$\mathbf{q} \in H(\text{div}; \Omega) : \mathbf{q} \cdot \mathbf{n} = \bar{q} \text{ on } \Gamma_q$
Lagrange multiplier $\lambda$	Scalar	$\lambda \in H^1(\Omega) : \lambda = 0 \text{ on } \Gamma_T$	$\lambda \in L^2(\Omega)$
Lagrange multiplier $\boldsymbol{\tau}$	Vector	Not used	$\boldsymbol{\tau} \in H(\text{div}; \Omega) : \boldsymbol{\tau} \cdot \mathbf{n} = 0 \text{ on } \Gamma_q$

Table 2: Function spaces for the stronger and weaker data-driven formulations.  $L^2(\Omega)$  and  $\mathbf{L}^2(\Omega)$  are the Lebesgue spaces for square-integrable scalar and vector functions, respectively.  $H^1(\Omega)$  is the Sobolev space for square-integrable scalar functions with square-integrable derivatives.  $H(\text{div}; \Omega)$  is the Sobolev space for square-integrable vector functions with square-integrable divergence.

### 3.1. Stronger data-driven formulation

Stronger mixed formulation for data-driven approach has been derived, tested and extended for elasticity and inelasticity in (Kirchdoerfer and Ortiz, 2016, 2017), while a similar formulation for diffusion problems was discussed in (Nguyen et al., 2020) and recently in (Kuliková et al., 2021). Following these works, a DD version for heat transfer including temperature  $T$  as one of the dataset  $\mathcal{D}$  variables is derived here.

The solution of the problem (1)-(2), supplemented by a dataset generated and handled as discussed in Section 2, can be found upon the minimisation of the functional (5) with the conservation law (1) imposed as a constraint. Therefore, we formulate a Lagrangian:

$$\mathcal{L}(\nabla T, \mathbf{q}, \lambda) = J(\nabla T, \mathbf{q}) + \int_{\Omega} \lambda (\nabla \cdot \mathbf{q} - s) d\Omega, \quad (6)$$

where  $\lambda$  is the field of scalar Lagrange multipliers. While the Dirichlet boundary condition on temperature (2b) is satisfied a priori, the Neumann boundary condition on flux (2a) can be enforced in the integral sense using the integration by parts of the term representing the constraint in the Lagrangian (6) and imposing  $\lambda = 0$  on  $\Gamma_T$ , see (Nguyen et al., 2020):

$$\begin{aligned} \mathcal{L}(\nabla T, \mathbf{q}, \lambda) &= J(\nabla T, \mathbf{q}) + \int_{\Omega} \nabla \lambda \cdot \mathbf{q} d\Omega - \int_{\Gamma_q} \lambda \mathbf{q} \cdot \mathbf{n} d\Gamma \\ &= \int_{\Omega} S_g (\nabla T - \mathbf{g}^*)^2 d\Omega + \int_{\Omega} S_q (\mathbf{q} - \mathbf{q}^*)^2 d\Omega - \int_{\Omega} \nabla \lambda \cdot \mathbf{q} d\Omega + \int_{\Gamma_q} \lambda \bar{q} d\Gamma - \int_{\Omega} \lambda s d\Omega. \end{aligned} \quad (7)$$

The solution is found as a stationary point of the Lagrangian at which its variation vanishes:

$$\begin{cases} \int_{\Omega} S_g (\nabla T - \mathbf{g}^*) \cdot \nabla \delta T d\Omega = 0 & \forall \delta T \in H_0^1(\Omega) \\ \int_{\Omega} S_q (\mathbf{q} - \mathbf{q}^*) \cdot \delta \mathbf{q} d\Omega + \int_{\Omega} \nabla \lambda \cdot \delta \mathbf{q} d\Omega = 0 & \forall \delta \mathbf{q} \in \mathbf{L}^2(\Omega) \\ \int_{\Omega} \mathbf{q} \cdot \nabla \delta \lambda d\Omega - \int_{\Gamma_q} \bar{q} \delta \lambda d\Gamma + \int_{\Omega} s \delta \lambda d\Omega = 0 & \forall \delta \lambda \in H_0^1(\Omega), \end{cases} \quad (8)$$

where  $H_0^1(\Omega)$  is a space for square-integrable scalar functions with square integrable gradient and zero value on the boundary  $\Gamma_T$ , i.e.  $H_0^1(\Omega) = \{u \in H^1(\Omega) \mid u = 0 \text{ on } \Gamma_T\}$ . The unknown trial functions  $T, \mathbf{q}, \lambda$  belong to

Field	Approximation order	
	Stronger DD	Weaker DD
Temperature $T$	$p$	$p$
Gradient of temperature $\mathbf{g}$	Not used	$p + 1$
Heat flux $\mathbf{q}$	$p - 1$	$p + 1$
Lagrange multiplier $\lambda$	$p$	$p$
Lagrange multiplier $\boldsymbol{\tau}$	Not used	$p + 1$

Table 3: Approximation orders to satisfy inf-sub stability conditions; note that  $p$  is the approximation order for the temperature field  $T$  in both formulations.

the spaces shown in the ‘‘Stronger DD’’ column in Table 2.

The variational problem (8) can be discretised and solved using linear FEM. Here, we used hierarchical shape functions (Ainsworth and Coyle, 2003) for both continuous  $(T, \lambda)$  and discontinuous  $(\mathbf{q})$  field approximations, see (Kulikova, 2025) for more details. To satisfy LBB stability conditions (Boffi et al., 2013), the approximation orders have to be chosen as shown in Table 3, see the ‘‘Stronger DD’’ column.

This stronger data-driven formulation will serve as a basis for comparison with the weaker mixed data-driven formulation introduced in the next subsection.

### 3.2. Weaker data-driven formulation

The stronger data-driven formulation derived in subsection 3.1 is already mixed, i.e. contains multiple unknown fields belonging to different function spaces. To improve on the original formulation, more natural spaces for the heat transfer problem can be chosen for the unknown fields enabled by the weaker formulation, the advantages are explained later in this subsection.

First, to obtain a weaker mixed formulation (Boffi et al., 2013), a new variable  $\mathbf{g}$  is introduced as one of the unknown fields the finite element analysis will solve for using an additional equation:

$$\mathbf{g} = \nabla T. \quad (9)$$

The closest point search (4) is now rewritten in terms of the new variable  $\mathbf{g}$ :

$$\text{dist}(\{T, \mathbf{g}, \mathbf{q}\}, \mathcal{D}) = \min_{\{T^*, \mathbf{g}^*, \mathbf{q}^*\} \in \mathcal{D}} \sqrt{S_T (T - T^*)^2 + S_g (\mathbf{g} - \mathbf{g}^*)^2 + S_q (\mathbf{q} - \mathbf{q}^*)^2}. \quad (10)$$

Similarly, the integrated distance functional (5) becomes:

$$J(\mathbf{g}, \mathbf{q}) = \int_{\Omega} S_g (\mathbf{g} - \mathbf{g}^*)^2 d\Omega + \int_{\Omega} S_q (\mathbf{q} - \mathbf{q}^*)^2 d\Omega. \quad (11)$$

Next, the Lagrangian is formed by minimising the integrated distance functional (11), and imposing the energy conservation law (1) and the new variable definition (9) as constraints:

$$\mathcal{L}(\nabla T, \mathbf{g}, \mathbf{q}, \boldsymbol{\tau}, \lambda) = J(\mathbf{g}, \mathbf{q}) + \int_{\Omega} \boldsymbol{\tau} \cdot (\mathbf{g} - \nabla T) d\Omega + \int_{\Omega} \lambda (\nabla \cdot \mathbf{q} - s) d\Omega, \quad (12)$$

where  $\lambda$  and  $\boldsymbol{\tau}$  are scalar and vector fields of Lagrange multipliers, respectively.

The regularity requirement on the temperature field is weakened by integrating the component containing gradient of temperature  $\nabla T$  in (12) by parts, at the same time satisfying the Dirichlet boundary condition (2b) as natural and imposing  $\boldsymbol{\tau} \cdot \mathbf{n} = 0$  on  $\Gamma_q$ , cf. (7):

$$\begin{aligned} \mathcal{L}(T, \mathbf{g}, \mathbf{q}, \boldsymbol{\tau}, \lambda) &= \int_{\Omega} S_{\mathbf{g}} (\mathbf{g} - \mathbf{g}^*)^2 d\Omega + \int_{\Omega} S_{\mathbf{q}} (\mathbf{q} - \mathbf{q}^*)^2 d\Omega \\ &+ \int_{\Omega} \boldsymbol{\tau} \cdot \mathbf{g} d\Omega - \int_{\Gamma_T} (\boldsymbol{\tau} \cdot \mathbf{n}) \bar{T} d\Gamma_T + \int_{\Omega} (\nabla \cdot \boldsymbol{\tau}) T d\Omega \\ &+ \int_{\Omega} \lambda (\nabla \cdot \mathbf{q}) d\Omega - \int_{\Omega} \lambda s d\Omega. \end{aligned} \quad (13)$$

The choice of function spaces for the unknown fields in the weaker formulation, see Table 2, results in lower regularity of the solution, as spaces for  $T$  and  $\mathbf{g}$  do not require the result to be smooth between any inner boundaries. However, the continuity of the normal flux  $\mathbf{q}$  component is enforced across any inner boundaries. This choice of spaces is more natural for the transport problems such as heat transfer.

Again, the solution is found as a stationary point of the Lagrangian (13) at which its variation vanishes:

$$\left\{ \begin{array}{l} \int_{\Omega} \delta T (\nabla \cdot \boldsymbol{\tau}) d\Omega = 0 \quad \forall \delta T \in L^2(\Omega) \\ S_{\mathbf{g}} \int_{\Omega} \delta \mathbf{g} \cdot (\mathbf{g} - \mathbf{g}^*) d\Omega + \int_{\Omega} \delta \mathbf{g} \cdot \boldsymbol{\tau} d\Omega = 0 \quad \forall \delta \mathbf{g} \in \mathbf{L}^2(\Omega) \\ S_{\mathbf{q}} \int_{\Omega} \delta \mathbf{q} \cdot (\mathbf{q} - \mathbf{q}^*) d\Omega + \int_{\Omega} (\nabla \cdot \delta \mathbf{q}) \lambda d\Omega = 0 \quad \forall \delta \mathbf{q} \in \mathcal{Q}_0 \\ \int_{\Omega} \delta \lambda (\nabla \cdot \mathbf{q}) d\Omega - \int_{\Omega} \delta \lambda s d\Omega = 0 \quad \forall \delta \lambda \in L^2(\Omega) \\ \int_{\Omega} \delta \boldsymbol{\tau} \cdot \mathbf{g} + (\nabla \cdot \delta \boldsymbol{\tau}) T d\Omega - \int_{\Gamma_T} (\delta \boldsymbol{\tau} \cdot \mathbf{n}) \bar{T} d\Gamma = 0 \quad \forall \delta \boldsymbol{\tau} \in \mathcal{Q}_0, \end{array} \right. \quad (14)$$

where  $\mathcal{Q}_0$  is a space of square-integrable vectorial functions with square integrable divergence and zero normal component on the boundary  $\Gamma_q$ , i.e.  $\mathcal{Q}_0 = \{\mathbf{v} \in H(\text{div}; \Omega) \mid \mathbf{v} \cdot \mathbf{n} = 0 \text{ on } \Gamma_q\}$ . The unknown trial functions  $T, \mathbf{g}, \mathbf{q}, \lambda, \boldsymbol{\tau}$  belong to the spaces shown in the ‘‘Weaker DD’’ column in Table 2.

After discretisation of the domain, each field in variational problem 14 can be interpolated using hierarchical shape functions, available in MoFEM (Kaczmarczyk et al., 2020). In particular, we use discontinuous shape functions for  $T, \mathbf{g}$ , and  $\lambda$  fields and generalisation of the Brezzi-Douglas-Marini finite element (Boffi et al., 2013) for fields  $\mathbf{q}$  and  $\boldsymbol{\tau}$ , see (Kulikova, 2025) for more details. Finally, it is important to note that the approximation orders are assigned to unknown fields as shown in Table 3 to satisfy LBB stability conditions (Boffi et al., 2013).

### 3.3. Iterative process and stopping criterion

Solving the problem using the data-driven method in either strong and weak formulation is an iterative procedure, where each iteration includes two steps:

1. Searching the dataset for the closest material point at every integration point using (4) in case of strong formulation or (10) in case of the weaker formulation.
2. Solving the finite element problem defined by (8) (stronger formulation) or (14) (weaker formulation).

In both cases, the iterative process requires a stopping criterion. The simplest one would be stop the process if the data search with (4) or (10) finds the same material datapoints at every integration point as in the previous iteration. However, in case of a large amount of datapoints being concentrated in a part of the dataset, more iterations do not necessarily provide better results.

Another option for a stopping criterion is comparing RMS measure of the distance between the field values and the dataset between the two iterations with a prior set tolerance:

$$\varepsilon_d(T, \mathbf{g}, \mathbf{q}) = \sqrt{\frac{1}{\mu(\Omega)} \int_{\Omega} (\text{dist}(\{T, \mathbf{g}, \mathbf{q}\}, \mathcal{D}))^2 d\Omega}, \quad (15)$$

where  $\mu(\Omega)$  is the area of the domain  $\Omega$  in a 2D case, and its volume in a 3D case. A stopping criterion based on choosing the same closest datapoints at all integration points twice (Kirchdoerfer and Ortiz, 2016; Nguyen et al., 2020), corresponds to setting the tolerance for  $\varepsilon_d(T, \mathbf{g}, \mathbf{q})$  to zero in (15).

### 3.4. Computational complexity

To finish the discussion of the data-driven framework, we briefly compare the computational complexity of the proposed method with the standard finite element approach to nonlinear problems using the Newton-Raphson scheme (Bonet and Wood, 1997).

For the nonlinear FE formulation, at each Newton-Raphson iteration, a global system is assembled and solved. Assuming an efficient sparse direct solver (Amestoy et al., 2000), the matrix inversion scales as  $\mathcal{O}(n_{\text{dof}}^{3/2})$ , where  $n_{\text{dof}}$  is the number of degrees of freedom. With  $N_{\text{NR}}$  Newton-Raphson iterations, the total complexity becomes:

$$\mathcal{O}(N_{\text{NR}} \cdot n_{\text{dof}}^{3/2}). \quad (16)$$

In contrast, the data-driven formulations have a constant diffusivity matrix requiring only a single matrix inversion:  $\mathcal{O}(n_{\text{dof}}^{3/2})$ . However, an iterative process which includes searching for a closest material datapoint for each integration point is performed. In our implementation, a nearest-neighbour search is carried out at every integration point using an R-tree (Guttman, 1984), yielding a search cost of  $\mathcal{O}(n_{\text{int}} \cdot \log n_{\text{mat}})$ , where  $n_{\text{int}}$  is the number of integration points and  $n_{\text{mat}}$  the number of material data points. With  $N_{\text{DD}}$  iterations, the total complexity is:

$$\mathcal{O}(n_{\text{dof}}^{3/2}) + \mathcal{O}(N_{\text{DD}} \cdot n_{\text{int}} \cdot \log n_{\text{mat}}). \quad (17)$$

The resulting computational cost difference between the standard and data-driven formulations depends on the size of the problem ( $n_{\text{dof}}$  and  $n_{\text{int}}$ ), the size of the material dataset ( $n_{\text{mat}}$ ), and the number of iterations required for convergence ( $N_{\text{NR}}$  or  $N_{\text{DD}}$ ). Larger problems with more degrees of freedom and integration points might perform faster with the data-driven approach, especially if the material dataset is small, as it avoids the need for multiple matrix inversions. On the contrary, small problems with fewer degrees of freedom and integration points will likely perform faster with the standard approach, especially if the material dataset is large.

The bottleneck of the data-driven approach is the search through the material dataset, which can be minimised by using efficient data structures (e.g., R-trees) and search algorithms. Additionally, to ensure the minimum number of integration points, the error indicators leading to adaptive refinement strategies, discussed in section 5, enabled by the weaker data-driven formulation are advantageous.

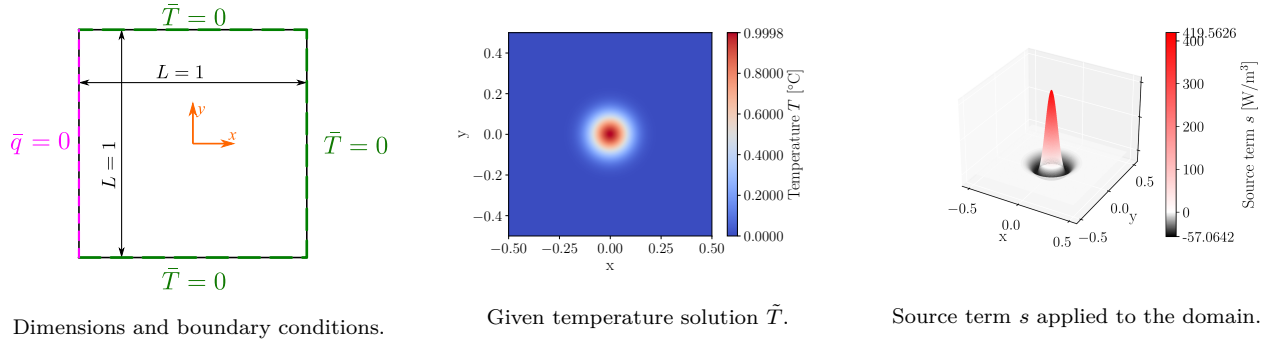


Figure 4: Example Exp-Hat: Analysis setup which corresponds to the exact solution  $\tilde{T} = e^{-100(x^2+y^2)} \cos \pi x \cos \pi y$ .

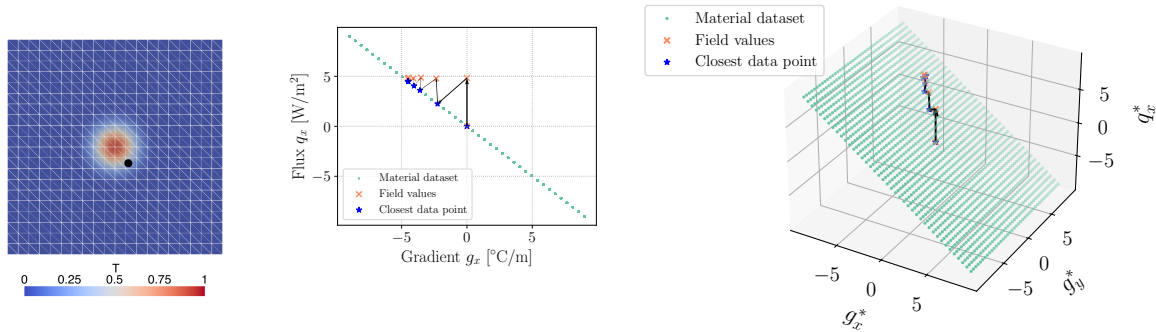


Figure 5: Path of an integration point (marked black in the domain on the left), which includes finding the closest point in the dataset (“Closest data point”) and projecting it onto a set where conservation laws and boundary conditions are satisfied (“Field values”). The problem is solved using weaker DD formulation (14) with mesh size  $h = 0.05$ , approximation order  $p = 2$ , and dataset including  $41^4$  material datapoints.

#### 4. Verification of stronger and weaker DD formulations w.r.t. analytical solution

To verify the implementation of the data-driven formulation discussed in section 3, a diffusion problem in a square 2D domain is considered, see Figure 4. The same example will be used in Section 5 to demonstrate the effectiveness of the adaptive refinement driven by the error estimators discussed in the same section.

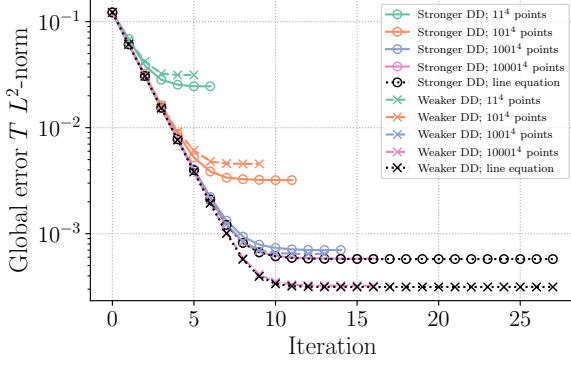
For testing purposes, we constructed the problem for a given solution of temperature  $\tilde{T}(x, y)$ :

$$\tilde{T}(x, y) = e^{-100(x^2+y^2)} \cos \pi x \cos \pi y, \quad (18)$$

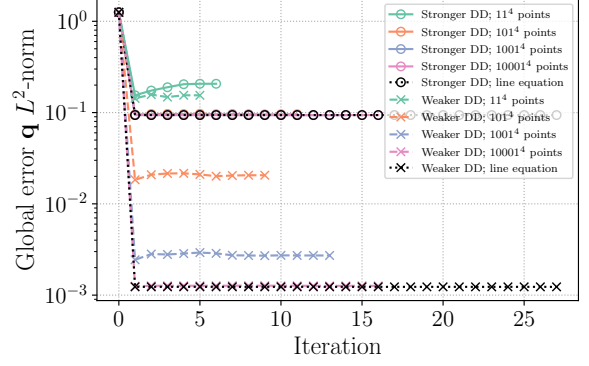
from which the applied source term  $s(x, y)$  and boundary conditions for heat flux  $\bar{q}$  and temperature  $\bar{T}$  are derived. The example was chosen due to the high localised gradients which cause numerical difficulties and high finite element approximation errors with low order approximations. For this example, thermal conductivity  $k = 1 \text{ W}/(\text{m} \cdot ^\circ\text{C})$  is used and the analysis setup with the exact solution are shown in Figure 4.

To solve the problem with the data-driven approach, material dataset is artificially generated using the exact solution  $\tilde{T}$ , its gradient  $\nabla \tilde{T}$  and flux  $\mathbf{q}$  derived with linear constitutive behaviour  $k = 1 \text{ W}/(\text{m} \cdot ^\circ\text{C})$  at regular intervals within prescribed ranges, see Figure 2(a) for an example dataset. The material dataset  $\mathcal{D} = \{g_x^*, g_y^*, q_x^*, q_y^*\}$  in this example does not contain values for  $T^*$ , and therefore the terms containing  $T^*$  in (4) or (10) are ignored. The iterative process discussed in subsection 3.3 is shown for one integration point in Figure 5.

Next, the material dataset  $\mathcal{D}$  is generated multiple times with increased density of datapoints in  $[-9, 9]$

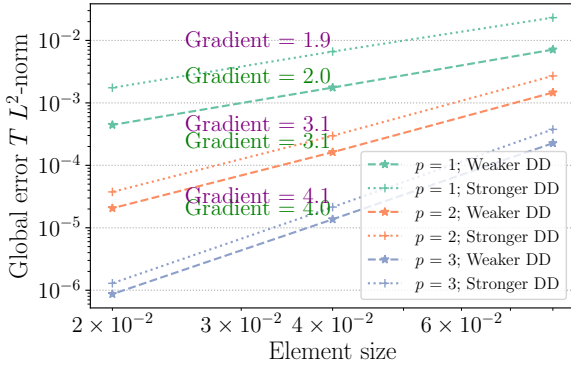


Global temperature error.

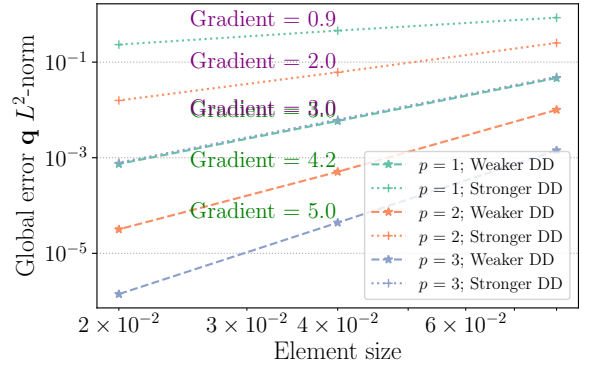


Global flux  $\mathbf{q}$   $L^2$ -norm.

Figure 6: Convergence of the global error norms w.r.t. the number of points in a material dataset  $\mathcal{D}_{4D}$  ( $h = 0.05$ ,  $p = 2$ ).



(a) Global temperature  $T$  error  $L^2$ -norm.



(b) Global flux  $\mathbf{q}$  error  $L^2$ -norm.

Figure 7: Comparison of the convergence of weaker and stronger DD solutions with “fully saturated dataset” to the exact solution.

range for  $g_x^*$  and  $g_y^*$ . The global error  $L^2$  norm of the  $T$  and  $\mathbf{q}$  fields is computed with respect to the exact solution. Furthermore, the results are compared to the case of the “fully saturated dataset”, that is, when the data search (4) or (10) is replaced by finding a closest point on a line  $\mathbf{q}^* = -\mathbf{g}^*$ , see Appendix B for more details. If no noise is present in the material dataset, the resulting global error converges with the increase in the number of material datapoints in dataset  $\mathcal{D}$ , see Figure 6. Note that the stronger and weaker DD formulations converge to different values of the global error norms. In particular, the resulting error in the case of the “fully saturated dataset” with no noise corresponds to the finite element approximation error, which differs between the stronger and weaker formulations.

The convergence of the DD solutions using the “fully saturated dataset” to the exact solution with decreasing element size and increasing approximation order is shown in Figure 7. The agreement between the convergence orders apparent in the slopes in Figure 7 and *a priori* error estimates shown in Table 4 demonstrate that the stronger and weaker data-driven approaches with saturated datasets have the same convergence rates as the standard and mixed FE formulations without the data-driven approach (Boffi et al., 2013).

The temperature  $T$  field converges to the exact solution with the same order for both stronger and weaker

Error norm	Convergence order	
	Standard FEM	Mixed FEM
$\ \tilde{T} - T^h\ _{L^2(\Omega)}$	$p + 1$	$p + 1$
$\ \tilde{\mathbf{q}} - \mathbf{q}^h\ _{\mathbf{L}^2(\Omega)}$	$p$	$p + 2$

Table 4: *A priori* error estimates for standard and mixed FEM formulations without the data-driven approach (Boffi et al., 2013). Note that  $p$  is the approximation order of the temperature field in both formulations.

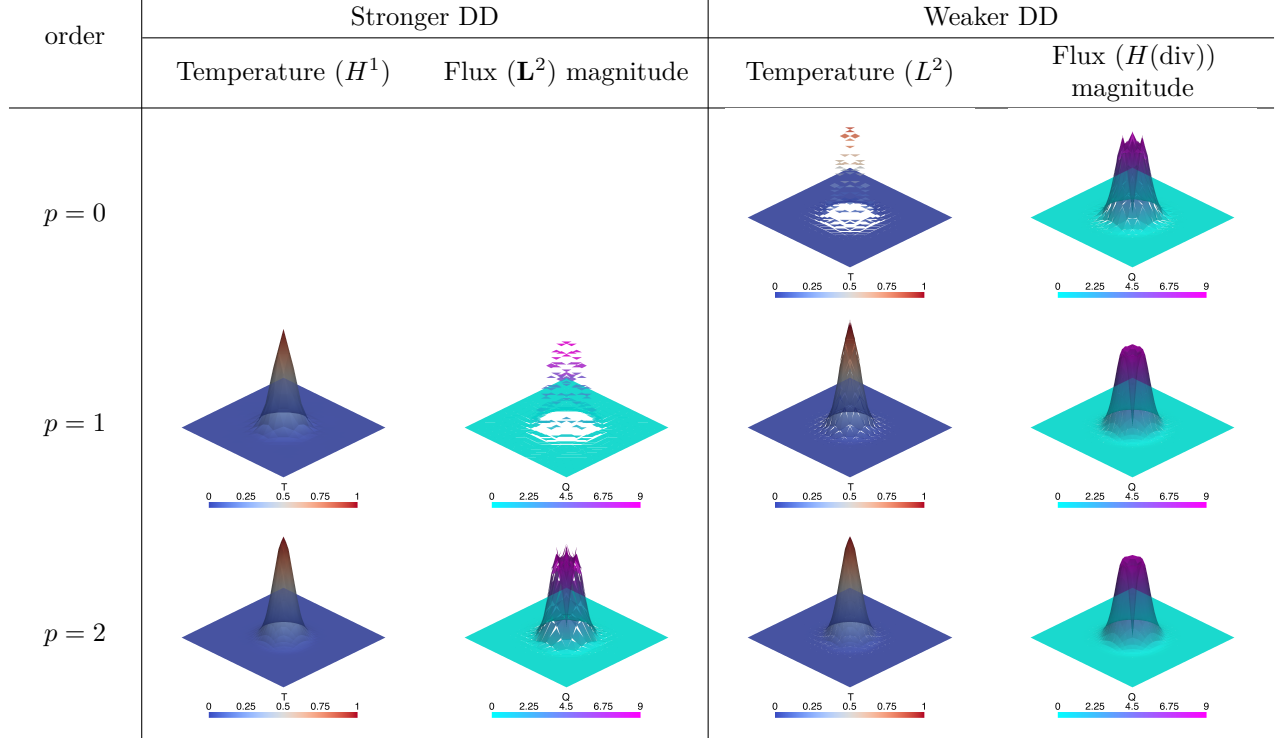


Table 5: Comparison of fields for different approximation orders between the stronger and weaker DD formulations ( $h = 0.05$ ). Note that  $p$  is the approximation order of the temperature field in both formulations.

formulations, however, since  $T \in L^2$  in the weaker formulation, approximation order  $p = 0$ , i.e. temperature is allowed to be a constant per element, see Figure 7(a) and Table 5. Note that while the approximation of the field  $T$  in  $L^2$  space allows for jumps between the element boundaries, these jumps decrease with higher approximation orders, provided that the source term applied to the problem is sufficiently regular. On the other hand, the convergence of the heat flux  $\mathbf{q}$  in the weaker formulation is two orders higher compared to the stronger formulation, see Figure 7(b) and Table 5.

## 5. Adaptive $hp$ -refinement with *a posteriori* error indicators

Numerical solution obtained with the finite element method contains FE approximation errors. Refining mesh or increasing approximation order on the elements with high values of error indicators aims to reduce the FE approximation errors with minimal increase in the problem size and simulation runtime. Adaptive refinement algorithm will be discussed in the following subsections, and, in addition, numerical errors and uncertainties related to the material dataset will be addressed in subsection 5.2.

### 5.1. Finite element approximation error indicators

Multiple ways to calculate FE approximation error indicators and estimates were proposed in literature (Oden et al., 1989; Repin, 2008; Grätsch and Bathe, 2005). For the weaker mixed DD formulation considered here, due to the temperature  $T$  and flux  $\mathbf{q}$  belonging to different function spaces, error indicators and estimators with little extra computational cost are available (Ainsworth, 2008; Braess and Verfürth, 1996; Carstensen, 1997). The particular *a posteriori* error indicators and error estimate calculated in this paper follow Braess and Verfürth (1996).

Error indicators “indicate” where the approximation errors discoverable by that particular indicator are the highest, however, any one error indicator might not capture all of the finite element approximation errors on its own. Therefore, the error estimate introduced in this section is composed of error indicators associated with temperature gradient, flux divergence, and jumps of values across the inner boundaries between elements, each of which is described in the following subsections.

#### 5.1.1. Error indicator associated with temperature gradient

The first error indicator is associated with the temperature gradient  $\nabla T$ . Since temperature  $T$  is approximated in  $L^2$  space, the field is not enforced to be continuous. Nevertheless, given that in the FE approach the fields are approximated using polynomial shape functions, even if the temperature field is not continuous between elements, the gradient of the corresponding polynomial approximation  $T^h$  can be readily computed at each element’s integration points *a posteriori*. The temperature gradient is then compared to the field  $\mathbf{g}$ , which represents the gradient of temperature as well, see (9). The error indicator  $\eta_e(\nabla T, \mathbf{g})$  is computed over a finite element  $\Omega_e$  as follows:

$$\eta_e(\nabla T, \mathbf{g}) = \|\nabla T - \mathbf{g}\|_{\Omega_e}^2. \quad (19)$$

The magnitudes of the fields for the problem considered in section 4, shown in Figure 8(a) and (b), should theoretically have the same values since they both represent the gradient of temperature. However, due to the finite element approximation satisfying the relation (9) in a weak sense, the values differ and produce the error indicator  $\eta_e$ , see Figure 8(c). Moreover, while the temperature field is approximated with order  $p$  shape functions, the gradient field  $\mathbf{g}$  is approximated with the higher approximation order,  $p + 1$ . Therefore, the resulting field  $\mathbf{g}$  is much smoother than the computed gradient of temperature  $\nabla T$ .

#### 5.1.2. Error indicator associated with flux divergence

The second error indicator is associated with the flux divergence  $\nabla \cdot \mathbf{q}$ . The error indicator  $\Omega_e$  measures the difference between the source term  $s$  and the divergence of the flux  $\nabla \cdot \mathbf{q}$ , which corresponds to the conservation of energy (1), and is computed over a finite element  $\Omega_e$  as follows:

$$\nu_e(\mathbf{q}) = h\|s - \nabla \cdot \mathbf{q}\|_{\Omega_e}^2, \quad (20)$$

where  $h$  is the representative size of the element  $\Omega_e$ . The values of the indicator  $\nu_e(\mathbf{q})$  are shown in Figure 9(a).

#### 5.1.3. Jump across the inner boundaries

Since the temperature field  $T$  is in  $L^2$  function space, the finite element solution is not continuous and jump of the field values across the inner boundaries can be calculated. For visual representation of the

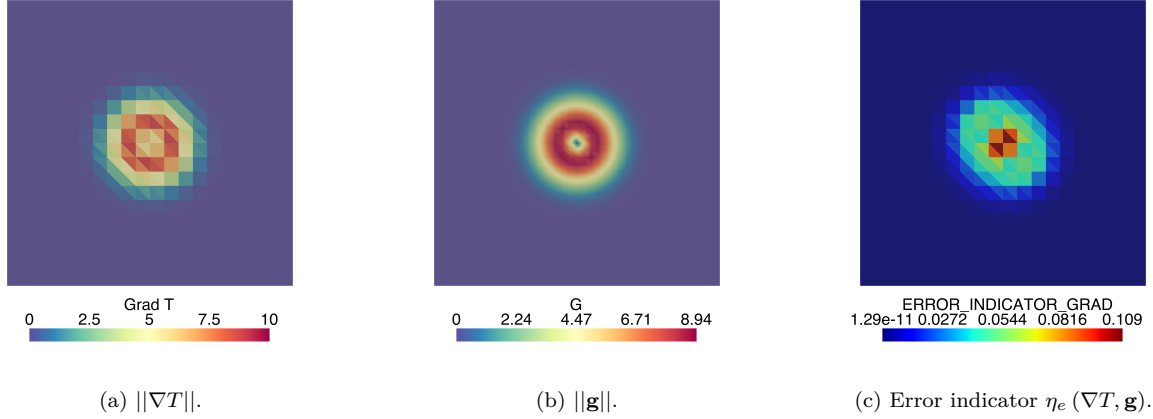


Figure 8: Comparison of the magnitudes of the gradient of temperature  $\nabla T$  (a) and the gradient field  $\mathbf{g}$  (b) for approximation order  $p = 1$  and element size  $h = 0.05$ . (c) The error indicator associated with temperature gradient  $\eta_e(\nabla T, \mathbf{g})$ , see (19).

temperature field values and the jumps between elements see Table 5 and Figure 9(b) respectively. A part of the jump error indicator,  $\gamma_l(T)$ , is computed over any inner boundary  $\Gamma_l$  as follows:

$$\gamma_l(T) = h^{-1/2} \|J(T)\|_{0,l}, \quad (21)$$

where  $J(T)$  is the jump of the temperature field  $T$  across one of the inner boundaries  $\Gamma_l$  belonging to an element  $\Omega_e$  and  $h$  is the representative size of the element  $\Omega_e$ . The jump error indicator  $\gamma_e(T)$  for the element is computed by summation of the jumps  $\gamma_l(T)$  across all boundaries associated with that element:

$$\gamma_e(T) = \sum_{l=1}^{n_{\Gamma_e}} \gamma_l(T). \quad (22)$$

However, the exact solution for the field  $T$  does not allow discontinuities. The error indicator can be used to identify elements where the jump in the temperature field is too high and where the refinement might be needed to achieve convergence towards the exact continuous solution.

#### 5.1.4. Error estimator

The complete error estimator (Braess and Verfürth, 1996) is a combination of the error indicators associated with temperature gradient (19), flux divergence (20), and jumps across the inner boundaries (22):

$$\mu_e = (\eta_e^2 + \nu_e^2 + \gamma_e^2)^{1/2}. \quad (23)$$

The global error estimator can be computed as:

$$\mu_g = \left( \sum_{e \in \Omega} [\eta_e^2 + \nu_e^2] + \sum_{l \in \Gamma} \gamma_l^2 \right)^{1/2}, \quad (24)$$

where  $\Gamma$  refers to all inner boundaries.

The error estimator (23) can also be extended to calculate the lower and upper bounds of the numerical

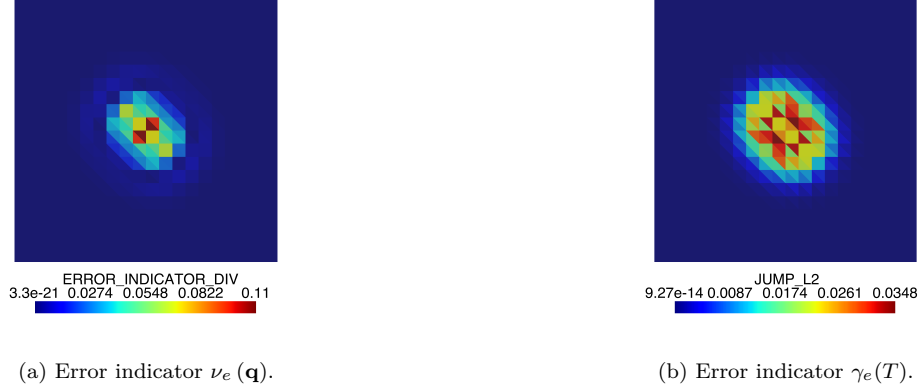


Figure 9: Error indicators assessing (a) the conformity of the numerical solution to the conservation of energy equation and (b) evaluating the jumps of temperature values.



Figure 10: Comparison of a combined error estimator  $\mu_e$  (left) and total error w.r.t. the exact solution (18) (right) on element basis.

error (Braess and Verfürth, 1996). The resulting error estimator and total error w.r.t. analytical solution

$$e_{\text{tot}} = \|T - \tilde{T}\|_{1,\Omega_e} + \|\mathbf{q} - \tilde{\mathbf{q}}\|_{0,\Omega_e}, \quad (25)$$

which is the sum of the  $H^1$ -norm of the temperature error and  $L^2$ -norm of the flux error;, are shown in Figure 10.

### 5.1.5. Error indicators with imperfect material dataset

The error estimator (23) can be used to identify elements where the solution is not well approximated and where the refinement is likely to improve the numerical solution accuracy. However, the data-driven approach uses a dataset which is rarely as perfect as shown in the previous section. Therefore, the error estimator (23) can only be seen as another error indicator for the DD approach since it does not take into account the uncertainties related to the material dataset. Nevertheless, for the purpose of brevity,  $\mu$  will continue to be referred to as an error estimator in the following sections.

To test this, a *tweaked* dataset is created with  $10^5$  material datapoints in the same way as Figure 2(a), having a set of datapoints with values of temperature gradient in  $x$ -direction in the range  $[-6, -5]$  removed,

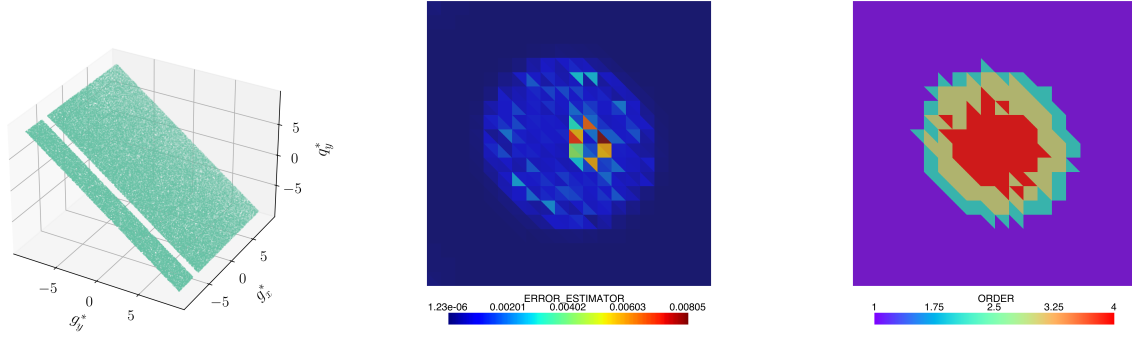


Figure 11: *Tweaked* dataset created with  $10^5$  material datapoints, having a set of datapoints with values of the temperature gradient in  $x$ -direction in the range  $[-6, -5]$  removed (left). Error estimator  $\mu_e$  (middle) and approximation order  $p$  (right) per element for the weaker data-driven formulation with missing data after adaptive order refinement.

resulting in a controlled form of missing data. An adaptive order refinement is performed six times by increasing the approximation order by one where the error estimator  $\mu_e$  is higher than the average error estimator:

$$p_e := \begin{cases} p_e + 1 & \text{if } \mu_e > \mu_{\text{avg}} \\ p_e & \text{otherwise} \end{cases} \quad (26)$$

where  $\mu_{\text{avg}}$  is the average error estimator over all elements:

$$\mu_{\text{avg}} = \frac{1}{N} \sum_{n=1}^N \mu_e^n, \quad (27)$$

where  $N$  is the total number of elements, and  $\mu_e^n$  is the value of the error estimator for the element  $n$ .

The error estimator  $\mu_e$  and the approximation order  $p$  per element shown in Figure 11, highlight that increasing the approximation order on the elements with high error estimators does not necessarily lead to a more accurate result. The element highlighted by the error estimator  $\mu_e$  have values within the  $[-6, -5]$  range of the temperature gradient in  $x$ -direction, which have been removed from the material dataset.

Therefore, the error estimator lacks the information about whether the errors are related to the FE approximation or to the material dataset if imperfections such as noise or missing data are present. Therefore, the relation to the material dataset should also be taken into account in the adaptive refinement process, which is discussed in the following subsection.

## 5.2. Data-driven error indicators

When elements with elevated error indicators due to the material dataset issues are refined (both in terms of element size and approximation order), more accurate result is not guaranteed. In particular, increasing the polynomial order of shape functions can lead to unwanted overfitting of the result to an imperfect material data. To prevent such overfitting, additional error indicators are proposed here to be included in the adaptive refinement: the average distance to the material dataset and the standard deviation of the distance to the dataset per element.

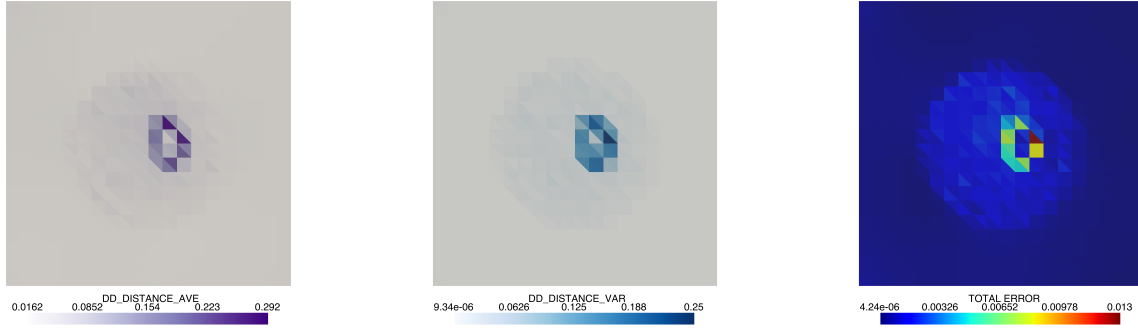


Figure 12: Average distance to the material dataset  $d_{ave}$  (left), standard deviation of the distance to the material dataset  $d_{std}$  (middle), and total error w.r.t. the exact solution (right) per element for the weaker data-driven formulation with missing data after adaptive order refinement.

### 5.2.1. Distance to the material dataset per element

The distance of the results to the material dataset, which will be denoted hereinafter as  $d$ , is calculated while finding the closest points in the dataset  $\mathcal{D}$  for every integration point using (4) or (10). To identify problematic elements, average of the distances per element is calculated as follows:

$$d_{ave} = \frac{\sum_{g=1}^G d_g}{G}, \quad (28)$$

where  $G$  is the number of integration points per the considered element. For visualisation of the average distance to the material dataset per element, see Figure 12(a).

If the average distance to the material dataset is *too high*, the element is deemed to be poorly informed of the material properties and further approximation order refinement would be overfitting the result. More discussion on what is *too high* is given in subsection 5.2.3.

### 5.2.2. Standard deviation of the distance to the material dataset per element

On the other hand, let us consider an element one part of which is well informed of the material properties, and another part is not. Consider the example in Figure 11, where data is missing in a localised area. Due to the size of the elements highlighted by the error estimator  $\mu_e$ , the missing material datapoints affect only a part of the element, i.e. some of the integration points have high distance to the dataset  $d$ , while others have low distance, while the average distance to the dataset  $d_{ave}$  might be similar to other elements. To identify such a case, the standard deviation of the distance to the material dataset per element is calculated:

$$d_{std} = \sqrt{\frac{\sum_{g=1}^G (d_g - d_{ave})^2}{G}}, \quad (29)$$

where  $d_{ave}$  is defined by (28). For visualisation of the standard deviation of the distance to the material dataset per element, see Figure 12(b).

It can be seen in Figure 12(c) that after the adaptive order refinement, the total error w.r.t. the exact solution is still present for elements where the dataset is far from the field values. Highlighting the high

standard deviation of the distance per element, we can also determine which parts of these elements are better informed (i.e. have smaller distance) of the material properties than others. Therefore, refining the mesh on such element is beneficial for better understanding the influence of the material dataset on the results.

### 5.2.3. Comparative measurement of the distance to the material dataset

To address the question of which values of the distance to the material dataset are *too high*, a comparative measurement  $\xi$  with the same units as  $d$  is needed, which represents RMS of the field values relevant for the material data search.  $\xi$  can either be calculated locally for each element or globally for the whole domain, representing relative or absolute distance comparative measures, respectively. Since in this case we are interested in high distances globally, a global  $\xi$  is defined as follows:

$$\xi = \left( \frac{\int_{\Omega} S_T T^2 d\Omega + \int_{\Omega} S_g \mathbf{g}^2 d\Omega + \int_{\Omega} S_q \mathbf{q}^2 d\Omega}{\mu(\Omega)} \right)^{1/2}, \quad (30)$$

where  $\mu(\Omega)$  is the area of the domain  $\Omega$  in a 2D case, and its volume in a 3D case. Note that (30) matches the units of distance in (4) and (10). Alternatively, if the relative distance to the dataset is of importance,  $\xi_e$  can be calculated and compared to on the element basis.

A new tolerance  $t_{ave}$  for the ratio of the average distance per element  $d_{ave}$  and the equivalent root mean squared measure  $\xi$  is introduced to determine which elements should not be taken into account for the adaptive  $p$ -refinement as follows: *Do not increase the approximation order of the element if:*

$$d_{ave} > t_{ave} \xi. \quad (31)$$

In a similar fashion, the standard deviation of the distance to the dataset  $d_{std}$  can be compared to  $\xi$ :

$$d_{std} > t_{std} \xi, \quad (32)$$

where  $t_{std}$  is another tolerance threshold related to the standard deviation of the distance (29) and the equivalent RMS measure (30). However, high standard deviation of the distance  $d$  within an element does not mean that refining the element mesh yields improved results or provides more information about the problem uncertainty. If an element where all of the values at the integration points are too far from the dataset is considered, i.e. have high distance  $d$ , refinement does not provide any advantage.

Therefore, an additional check is proposed which compares the values of the average and standard deviation in the element to evaluate if the refinement should take place:

$$d_{std} > t_{std}^{ave} d_{ave}, \quad (33)$$

where  $t_{std}^{ave}$  is another tolerance parameter.

### 5.3. Adaptive hp-refinement algorithm

The error indicators (19), (20), (22) and error estimator (23) are computed *a posteriori*, and highlight the elements with the highest FE approximation errors or the elements which are influenced by a less reliable part of the material dataset used. Since the elements flagged for the  $p$ -refinement by high error estimator with high distance to the material dataset are not well informed of the material properties, the approximation

order  $p$  is not increased for these elements and the values of the error estimator on these elements should not be included in calculation of the average error estimator  $\mu_{\text{avg}}$ . Therefore, we introduce *bounded* average error estimator  $\hat{\mu}_{\text{avg}}$ , which excludes the elements with high distance to the dataset:

$$\hat{\mu}_{\text{avg}} = \frac{1}{N} \sum_{n=1}^N \begin{cases} \mu_e^n, & d_{\text{ave}}^n \leq t_{\text{ave}} \xi \\ 0, & \text{otherwise,} \end{cases} \quad (34)$$

where  $d_{\text{ave}}^n$  is the average distance to the dataset for the element  $n$ .

Considering  $p$ -refinement in the domain where the finite element approximation errors are high,  $h$ -refinement in highlighted elements adjacent to the boundaries, and the elements with high standard deviation of the distance to the dataset, the adaptive refinement is performed as shown in Algorithm 1.

---

**Algorithm 1** Adaptive  $hp$ -refinement driven by error estimator and distance to the material dataset

---

- 1: Initialize with the lowest approximation order  $p = 1$  and the coarsest mesh.
  - 2: **repeat**
  - 3:     Solve the problem (14).
  - 4:     Calculate the error indicators and estimator (23).
  - 5:     Calculate the average error estimator (27) and bounded average error estimator (34)
  - 6:     Calculate the distance to the material dataset at every integration point (10)
  - 7:     Calculate the average distance  $d_{\text{ave}}$  per element (28)
  - 8:     Calculate the standard deviation of the distance  $d_{\text{std}}$  per element (29)
  - 9:     Calculate the comparative measurement  $\xi$  (30)
  - 10:    **if**  $\mu_e > \hat{\mu}_{\text{avg}} t_p$  **and**  $d_{\text{ave}} \leq t_{\text{ave}} \xi$  **then**
  - 11:        $p_e = p_e + 1$
  - 12:    **end if**
  - 13:    **if**  $\mu_e > \mu_{\text{avg}} t_h$  **and** element is adjacent to a boundary  $\Gamma$  corner  
       **or**  $\{d_{\text{std}} > t_{\text{std}} \xi$  **and**  $d_{\text{std}} > t_{\text{std}}^{\text{ave}} d_{\text{ave}}\}$  **then**
  - 14:       Refine mesh of this element.
  - 15:    **end if**
  - 16: **until** a specified number of refinements is reached.
- 

#### 5.4. Demonstration of the adaptive refinement with error indicators

The adaptive refinement is showcased on the Exp-Hat example with a *tweaked* dataset. The refinement utilises Algorithm 1 with tolerances defined in Table 6.

Figure 13 shows the snapshots of the refinement iterations, showing the distance to the material dataset at each integration point, its standard deviation per element, and the corresponding approximation order  $p$ . The algorithm is able to decrease the finite element approximation error where the knowledge of the material behaviour through the material dataset is high, while at the same time isolating the area with missing data by refining the mesh and keeping the approximation order low.

## 6. Validation with a graphite brick example

To validate the introduced approach, a 2D model of nuclear graphite brick used in Advanced gas-cooled reactors (AGR) is considered (Farrokhnia et al., 2022), obtained from the 3D geometry by assuming no variations of the fields along the vertical axis of the brick. Due to the symmetry and the boundary conditions, only a quarter of a horizontal brick slice is used in the numerical analysis, as shown in Figure 14. The inner boundary is kept at  $1000^\circ\text{C}$  to simulate the exposure to the heat from the nuclear fuel housed in the cylindrical

Condition	Threshold	Value	Refinement	Description
$\mu_e > \mu_{\text{avg}} t_p$	$t_p$	1.5	$p: \uparrow$	High error estimator: increase $p$
$d_{\text{ave}} > t_{\text{ave}} \xi$	$t_{\text{ave}}$	4	$p: \times$	Too far from dataset: prevent refinement
$d_{\text{std}} > t_{\text{std}} \xi$	$t_{\text{std}}$	0.5	$h: \uparrow$	High standard deviation: refine mesh
$d_{\text{std}} < t_{\text{std}}^{\text{ave}} d_{\text{ave}}$	$t_{\text{std}}^{\text{ave}}$	0.5	$h: \times$	Too far from dataset: prevent refinement
$\mu_e > \mu_{\text{avg}} t_h$	$t_h$	4	$h: \uparrow$	Threshold aimed at tackling flux singularities

Table 6: Threshold value for adaptive  $hp$ -refinement algorithm applied to example in Figure 13. Each condition determines whether to increase the polynomial order ( $p$ ), refine the mesh ( $h$ ), or suppress refinement based on error estimators and distance measures relative to the material dataset. The table is divided into three groups (separated by horizontal solid lines);  $\uparrow$  means an increase in the refinement, and  $\times$  overrules  $\uparrow$  within the group.

bore in the middle of the brick, while the outer boundary is kept at  $500^\circ\text{C}$  representing the exposure to the carbon dioxide gas acting as a coolant when the reactor is operational. These temperatures are chosen for testing purposes only as the temperatures for each of the graphite bricks vary throughout a nuclear reactor’s core. At the same time, it is assumed that there is no heat transfer through the small inner holes, which are filled with methane gas, a poor thermal conductor under reactor operating conditions.

For testing purposes, the material dataset, as described in Figure 2(b) and subsection Appendix A.2, is used. The material dataset is created through artificial experiments, and after the material datapoints were generated, a section of the dataset with  $g_x^*$  in the range  $[-9 \times 10^3, -6 \times 10^3]$  was removed. The artificial issue of missing data could represent equipment malfunction during testing, poor handling/preprocessing of the material datapoints, or simply not including the material states in the data gathering procedure.

Additionally, real material datasets always include noise, therefore, for the purpose of this example, white noise with normal distribution and standard deviation of  $\sigma_\eta = 10^6$  is added to the flux values in the  $y$ -direction for any points with temperature gradient magnitude less than  $2 \times 10^{-3}$ :

$$q_y^* := \begin{cases} q_y^* + \eta & \text{if } |\mathbf{g}^*| < 2 \times 10^3 \\ q_y^* & \text{otherwise,} \end{cases} \quad (35)$$

where  $\eta = \mathcal{N}(0, \sigma_\eta)$ . This scenario could represent a case when the measurement of small temperature gradient is difficult and/or inaccurate. The noise was only added to the flux values in the  $y$ -direction to evaluate the propagation of the noise to other dimensions.

The same refinement algorithm with the same tolerances as depicted in Algorithm 1 and Table 6 is used to refine the mesh and approximation order in the elements. The adaptive refinement is stopped after 3 iterations and the result is compared to the solution without any refinement in Figure 15. The approximation order was increased where the finite element approximation error was high within the domain and the distance to the material dataset was not *too high*. Additionally, it can be seen in Figure 15 that the mesh refinement captures the singularity of the heat flux and decreases the variance of the distance to the material dataset within elements.

The resulting fields are shown in Figure 16. The adaptive refinement is able to target the flux singularities in the corners of the graphite brick and refine the elements accordingly, see Figure 16(c). At the same time,

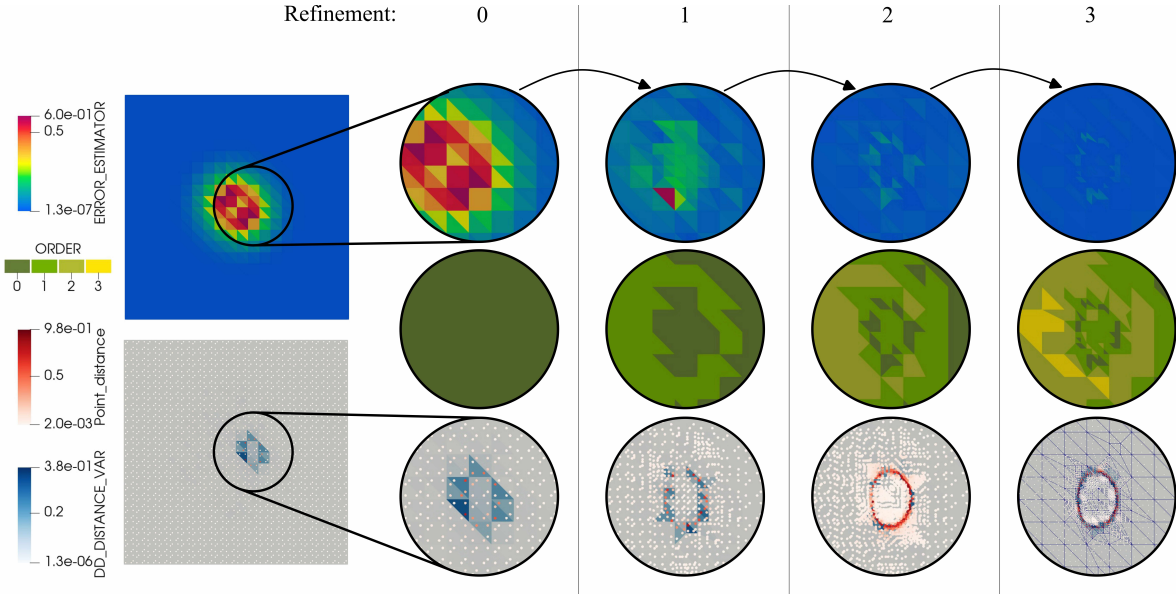


Figure 13: Snapshots of refinement iterations showing the error estimator, approximation order, distance to the material dataset at each integration point, and its standard deviation per element. The refinement utilises Algorithm 1 with tolerances defined in Table 6.

the area where the distance to the material dataset is high is isolated and the approximation order is kept low, therefore, the finite element approximation is not overfitted to imperfect data.

The values of the calculated fields can be extracted *a posteriori* w.r.t. the distance to the material dataset threshold (31) defining which points are “far” from the material dataset upon convergence, see Figure 17. The “far” material datapoints are located either

1. inside and around the area where the material datapoints were removed from the dataset, or
2. around the area where the noise has been added to the flux values in the  $y$ -direction.

The second case is related to the choice of the generation of the noise in the material dataset as there was no transition between the material datapoints with and without noise, therefore, it is likely that the jump between the noisy points and the non-noisy points at the border of the noisy area is lacking material datapoints. This is not necessarily physical, but rather a limitation of the dataset used, and can be imagined as two material datasets or two results of experiments are combined together, one with noisy flux values and another without

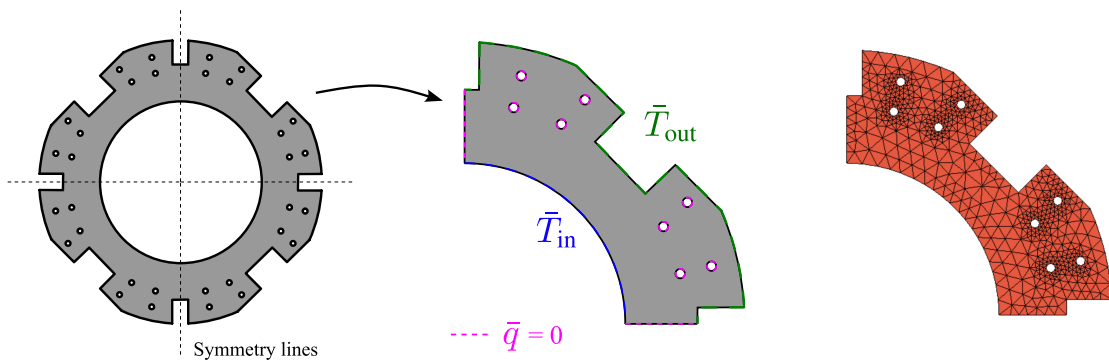


Figure 14: Geometry and mesh of a 2D model of nuclear graphite brick with boundary conditions of  $\bar{T}_{in} = 1000^{\circ}C$  and  $\bar{T}_{out} = 500^{\circ}C$  and  $\bar{q} = 0$  on the symmetry lines and the small inner holes.

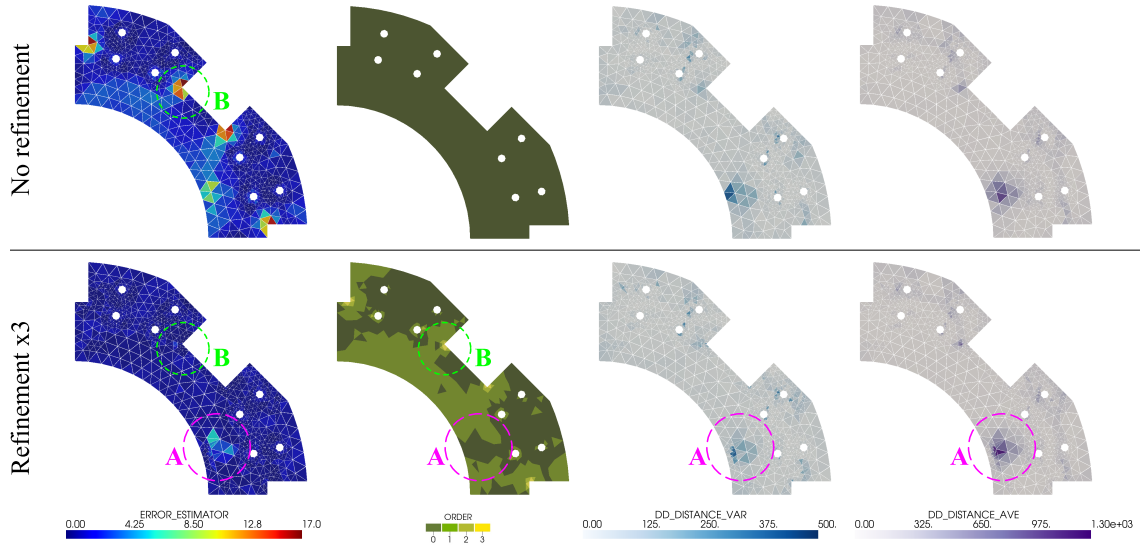


Figure 15: Comparison of the error indicators for the graphite brick example before and after using adaptive refinement algorithm, showing snapshots of the approximation order  $p_e$ , error estimator  $\mu_e$ , average and standard deviation of the distance to the material dataset,  $d_{ave}$  and  $d_{std}$ . In the figures, area A is the part of the domain where the field values are far from the dataset (since the dataset is missing data), and area B corresponds to one of the regions with flux singularity. The refinement utilises Algorithm 1 with tolerances defined in Table 6.

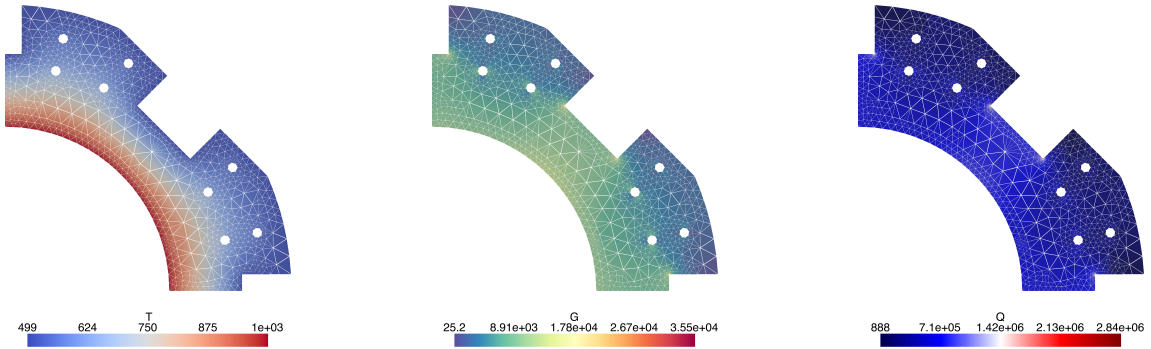


Figure 16: Results of the 2D brick slice example: temperature field  $T$  (left); temperature gradient field  $\mathbf{g}$  (centre); flux field  $\mathbf{q}$  (right).

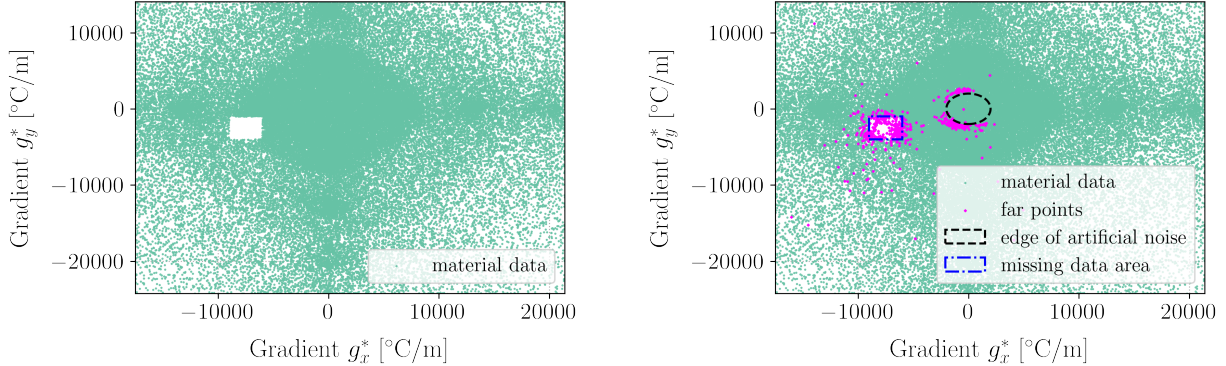


Figure 17: Material dataset with computed field values plotted for integration points which resulted in “far” distance to the material dataset, equivalent to (31) for integration points instead of elements.

noise.

In this section, we introduced several criteria to drive adaptive refinement, namely, finite element and distance error indicators. Application of the adaptive refinement algorithm reduces approximation errors and increases confidence in the predictions using an imperfect material dataset. However, the use of the material dataset in the solution enables multiple possible solutions to the problem which all satisfy the conservation laws and boundary conditions. Therefore, additional considerations are necessary to quantify the non-uniqueness of the solution caused by the dataset imperfections such as noise.

## 7. Quantification of non-uniqueness

The material dataset can contain noise or be missing data, and since there are multiple subsets of the material dataset which satisfy the conservation laws and boundary conditions, the solution is not unique. The certainty of the solution, therefore, depends on the quality of the material dataset w.r.t. the problem being solved. The uncertainty coming from the material dataset can be measured on the dataset level (preprocessing the material dataset), solution level (during the dataset search within the iterative process), or after the solution is obtained (postprocessing the results). It is important to highlight that the non-uniqueness of the solution resulting from the DD formulation is not an issue and instead can be quantified and used to indicate the uncertainty of the solution.

At the same time, it is important to differentiate between the uncertainties/errors spanning from the finite element approximation and the uncertainties/errors coming from the material dataset used. The adaptive refinement is therefore necessary to decrease the finite element approximation errors with minimal increase of the number of unknowns and integration points, which are closely related to the computational cost of the solution, see subsection 3.4 and (17).

To address the uncertainties related to the material dataset, non-uniqueness quantification based on Markov chain Monte Carlo (MCMC) analysis is proposed, see Algorithm 2. In this algorithm, the solution of the problem using adaptive refinement, as outlined in Algorithm 1, serves as a starting point of the statistical analysis. The resulting fields are then perturbed in a random direction by a perturbation value, which is normally distributed as:

$$\psi \sim \mathcal{N}(0, \kappa), \quad (36)$$

where  $\kappa$  is a metaparameter corresponding to the standard deviation of the perturbation value. The

---

**Algorithm 2** Markov chain Monte-Carlo Simulations
 

---

- 1: Initialize the fields.
  - 2: Solve the problem using the data-driven approach and adaptive refinement using Algorithm 1
  - 3: **repeat**
  - 4:   Solve the problem.
  - 5:   Save the fields.
  - 6:   Perturb the fields.
  - 7:   Use the perturbed fields as initial fields.
  - 8: **until** Monte-Carlo criteria are satisfied
  - 9: Calculate the average and standard deviation of the resulting fields.
- 

perturbation metaparameter  $\kappa$  can be chosen based on the average value of the field, the current local standard deviation of the field, the maximum value of the field, or the local or average distance to the material dataset, see (Kulikova, 2025) for more details.

The fields requiring perturbation are the fields that are being solved for and are at the same time used in the search for the closest material data points, i.e. the flux field  $\mathbf{q}$ , the gradient field  $\mathbf{g}$  and the temperature field  $T$ . The perturbed fields are then used as initial fields for the next Monte-Carlo iteration of the analysis. The mesh and the approximation order are unchanged between the iterations and remain the same as at the end of the adaptive refinement. After each solution, the resulting fields are saved and the process is repeated a number of times until the Monte-Carlo criteria are satisfied. The stopping criteria can be set to the number of iterations or the difference between the average standard deviation of the fields from the previous and the current iteration.

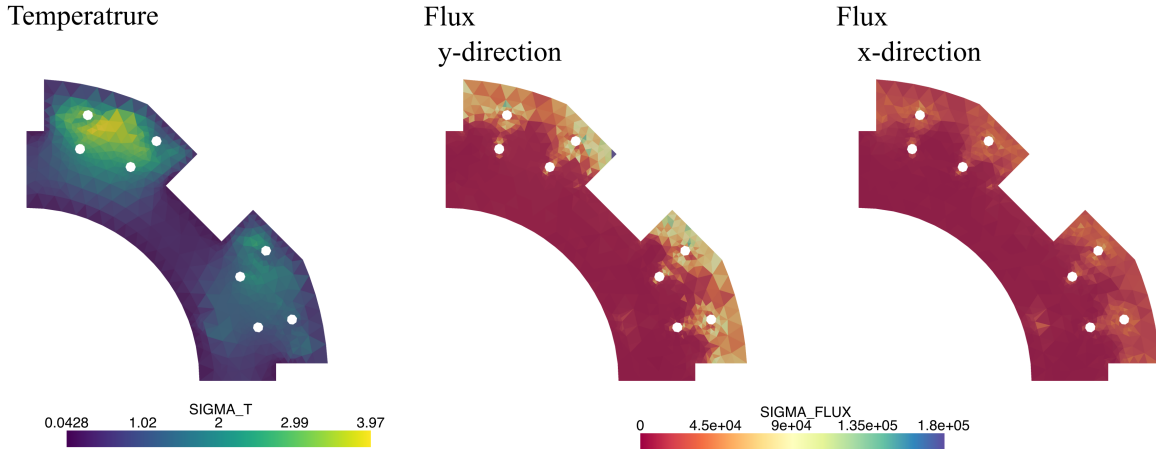


Figure 18: Standard deviation of the temperature  $T$  and flux  $\mathbf{q}$  fields after the adaptive refinement and Monte-Carlo simulations, showing the uncertainty of the solution w.r.t. the material dataset used. The standard deviation is calculated for each integration point and shown as a magnitude,  $x$ -component, and  $y$ -component of the flux field  $\mathbf{q}$ .

Since the resulting fields are collected and saved after each iteration, the standard deviation of the fields can be calculated. The integration scheme used for calculating the fields is Gauss quadrature, with standard Gauss points chosen based on the approximation order of the fields. In contrast, the field values used for statistical analysis are evaluated and stored at regularly spaced locations within each element, determined using Newton-Cotes quadrature. These Newton-Cotes points are not used for integration; rather, they serve only as evaluation points to simplify the computation of uncertainty due to non-uniqueness. In the example introduced,  $\kappa = 10^4$  and the Monte-Carlo simulations are stopped after 100 iterations. The values are chosen

to be high enough to perturb the fields significantly, but not too high to affect the number of iterations required to converge the DD iterative process for each Monte-Carlo iteration.

The results of the Monte-Carlo simulations are the average and the standard deviation of the fields evaluated on each regular evaluation point. The standard deviation is in the same units as the fields; hence, the interpretation is straightforward. Furthermore, the standard deviation of each field is summarised per element for ease of interpretation, see Figure 18 for the resulting standard deviation of the flux field  $\mathbf{q}$ . The standard deviation of the flux field in  $y$ -direction is higher than the standard deviation in  $x$ -direction, which is expected as the noise was added to the flux values in the  $y$ -direction, see (35). Nevertheless, the datapoints in the  $x$ -direction do not contain noise but the results in the  $x$ -direction are still affected by the noise in the  $y$ -direction.

## 8. Conclusion

This paper introduces a conservative data-driven finite element framework for solving heat transfer problems using material datasets directly in a simulation. The main novelty of this work is the proposed combination of the mixed finite element formulation and the data-driven approach. Mixed formulation uses the natural spaces for the unknown fields, allows for the jump of temperature between elements, and enforces the continuity of the normal flux component across any inner boundaries. Such a formulation provides naturally arising error indicators and estimator, which are used for adaptive refinement criteria.

The adaptive refinement algorithm was extended by calculating the variance of the distance to the material dataset within an element, which can be used together with the average distance to the material dataset per element to choose which elements should be refined. The error indicators introduced through the mixed formulation were adapted to the weaker data-driven approach. The analysis showed that the standard error indicators highlight not only where the finite element approximation is poor, which can be decreased by refinement, but also elements that use a problematic part of a material dataset. By using the proposed criteria for adaptive  $hp$  refinement and choosing where  $h$  and  $p$  refinement takes place independently of each other, the refinement is able to reduce the finite element approximation errors where the material dataset is relatively reliable and isolate areas where the material dataset is missing data.

Having used the adaptive refinement in the areas where it makes an impact on the accuracy, it is feasible to repeat the analysis multiple times with different initial field values to evaluate the uncertainty of the results. The final part of this work is devoted to quantifying the uncertainty of the resulting fields values using Monte-Carlo simulations, evaluating the standard deviation of the results, and interpreting the uncertainty in terms of the material dataset used. This approach makes it possible to differentiate between the errors coming from the finite element approximation and uncertainty related to sparse, missing or noisy parts of material dataset.

The method is fully tested using a 2D model of a nuclear graphite brick, where the material dataset is created through artificial experiments. The adaptive refinement is able to target the flux singularities in the corners of the graphite brick and refine the elements accordingly, while at the same time isolating the area with missing data by refining the mesh and keeping the approximation order low. Finally, the uncertainty of the solution is quantified using Markov chain Monte Carlo simulations, which provide a measure of non-uniqueness of the solution.

The proposed method is a step towards a more flexible and efficient way of solving nonlinear heat transfer problems with material datasets, which can be used in various applications, such as nuclear engineering,

materials science, and mechanical engineering. The method can be further extended to include more complex material datasets and to improve the adaptive refinement process.

## Appendix A. Dataset Creation

This appendix describes the details of the dataset creation process for the material dataset used in this work. Two ways are introduced: *regular* and *artexp*.

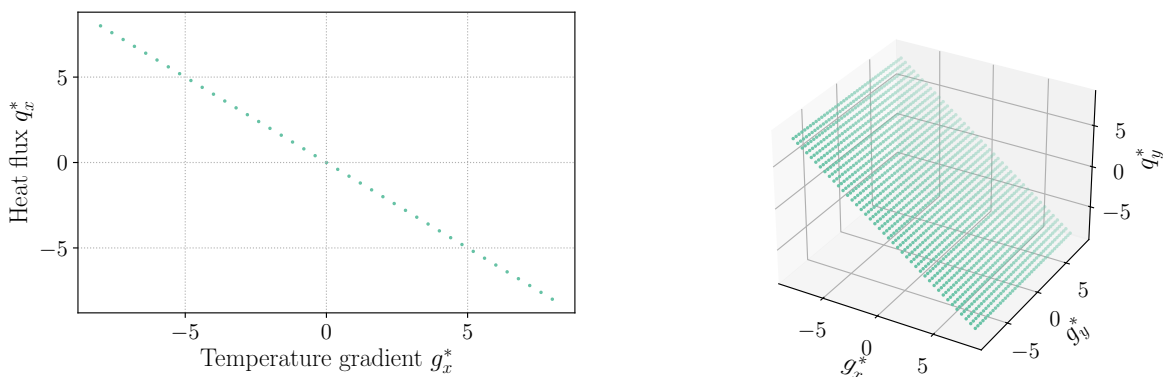
### Appendix A.1. Regular material dataset creation

The simplest material behaviour for heat diffusion follows Fourier’s law, where the heat flux  $\mathbf{q}$  is proportional to the negative gradient of the temperature  $\nabla T$ , given by

$$\mathbf{q} = -k\nabla T, \quad (\text{A.1})$$

where  $k$  is the thermal conductivity constant.

To introduce the data-driven method, a synthetic dataset is generated by considering temperature gradients  $\nabla T$  in the range  $[-A, A]$ , where the components  $g_x = \partial T/\partial x$  and  $g_y = \partial T/\partial y$  are sampled independently from a uniform distribution. The corresponding flux values are computed using the constitutive equation (A.1), resulting in a grid of material data points, as illustrated in Figure A.1.



Relation in the  $x$ -direction

3D view of the 4D material dataset

Figure A.1: Regular material dataset: Simplest grid material dataset  $\mathcal{D}$  with  $k = 1$ .

Algorithm A.1 outlines the algorithm for constructing this regular dataset. It iterates over the specified range of temperature gradients, computes the flux components  $q_x$  and  $q_y$ , and stores the resulting data points in the dataset  $\mathcal{D}_{4D}$ .

---

### Algorithm A.1 Creating a regular material dataset

---

- 1: Initialise an empty dataset  $\mathcal{D}_{4D}$
  - 2: **for** each temperature gradient  $g_x$  in the range  $[-A, A]$  with  $count_G$  equally spaced intervals **do**
  - 3:     **for** each temperature gradient  $g_y$  in the range  $[-A, A]$  with  $count_G$  equally spaced intervals **do**
  - 4:         Compute the flux components:  $q_x = -kg_x$ ,  $q_y = -kg_y$
  - 5:         Add the point  $(g_x, g_y, q_x, q_y)$  to the dataset  $\mathcal{D}_{4D} = \{\mathbf{g}^*, \mathbf{q}^*\}$
  - 6:     **end for**
  - 7: **end for**
-

### Appendix A.2. Artificial experiment material dataset creation

The primary application of the framework developed in this paper is the heat flow through graphite bricks used in advanced gas-cooled reactors (AGR) in the UK (Farrokhnia et al., 2022). Graphite bricks form the core of the reactor, providing structural support, and graphite also serves as a neutron moderator, slowing down fast neutrons during the operation. Graphite bricks experience changes in material properties over time, including a decrease in thermal conductivity, an increase in porosity, and density loss due to radiation exposure inside the nuclear reactor’s core (Kelly, 1982).

The principles discussed herein regarding nonlinear heat transfer in graphite bricks can also apply to other reactor components, such as boilers, or to entirely different contexts, such as building insulation or the diffusion of substances like algae in aquatic environments. The properties of graphite bricks, influenced by porosity, depend on factors including weight loss and microstructural changes resulting from irradiation duration and intensity, as well as the specific location within the reactor.

#### *Synthetic datasets for demonstration*

While this paper does not employ real experimental data for the properties of the graphite bricks, it will utilise synthetic datasets to demonstrate the capabilities of the developed data-driven approach. These synthetic datasets are generated through various synthetic experiments using one of multiple possible material models for heat transfer in graphite:

$$k(T) = 134.0 - 0.1074T + 3.719 \times 10^{-5}T^2, \tag{A.2}$$

where  $k$  [ $W/mK$ ] represents the thermal conductivity of the graphite brick, and  $T$  is the temperature in  $^{\circ}C$ . This model is derived from work conducted for high-temperature gas-cooled reactors, encompassing temperature ranges from room temperature to  $1000^{\circ}C$  (McEligot et al., 2016).

A synthetic experiment aims to replicate a real-life experiment on a piece of material considered, such as a piece of graphite used in a nuclear reactor. The geometry and mesh used for the synthetic experiment are shown in Figure A.2, and the analysis is performed with hierarchical shape functions with approximation order  $p = 2$  using a nonlinear formulation derived with the nonlinear heat conductivity (A.2), see Kulikova (2025) for the nonlinear formulation used. For an example setup, the temperature on the inner surface is kept at  $500^{\circ}C$  and on the outer surface at  $1100^{\circ}C$  for one of the experiments. More experiments are conducted with different inner and outer temperature for each instance of the experiment to cover the possible ranges of temperature, temperature gradient and flux graphite might reach in a nuclear reactor. The temperature, its gradient and flux are recorded at a set of points (integration points of Gauss quadrature).

The synthetic experiments simulate nonlinear material behaviour (see (A.2)) and apply the nonlinear heat diffusion formulation (Kulikova, 2025). These experiments are conducted over a temperature range of  $[400, 1100]$  by iterating through 10 equally spaced values for both  $\bar{T}_{in}$  and  $\bar{T}_{out}$  within this range. Each combination of  $\bar{T}_{in}$  and  $\bar{T}_{out}$  values is tested to produce the material dataset, shown in Figure A.3.

### Appendix B. Finding the closest point on a line

The data search described by (4) or (10), in case of "fully saturated" dataset, can be replaced by the search for the closest point on a curve corresponding to the conservation law equation (A.1). For simplicity,  $\nabla T = \mathbf{g}$ , and  $(\cdot)^*$  refers to the value on the line in this section.

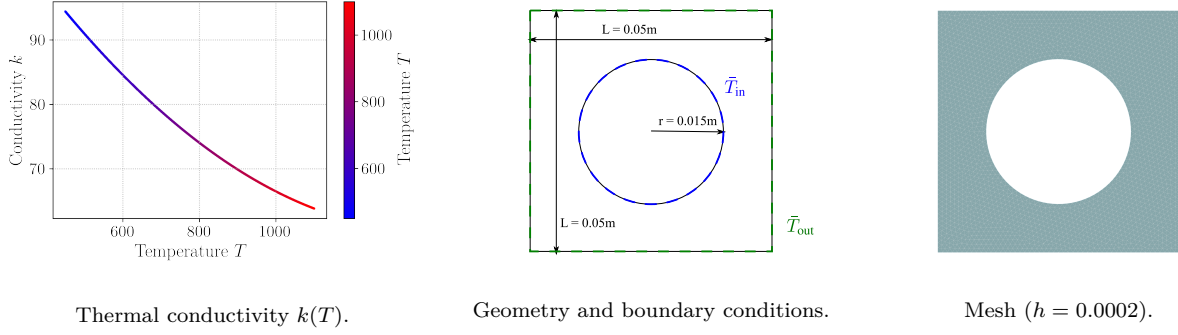


Figure A.2: Example Synthetic experiment: Geometry and mesh used for the synthetic experiment setup with  $\bar{T}_{in}$  and  $\bar{T}_{out}$  as temperature boundary conditions.

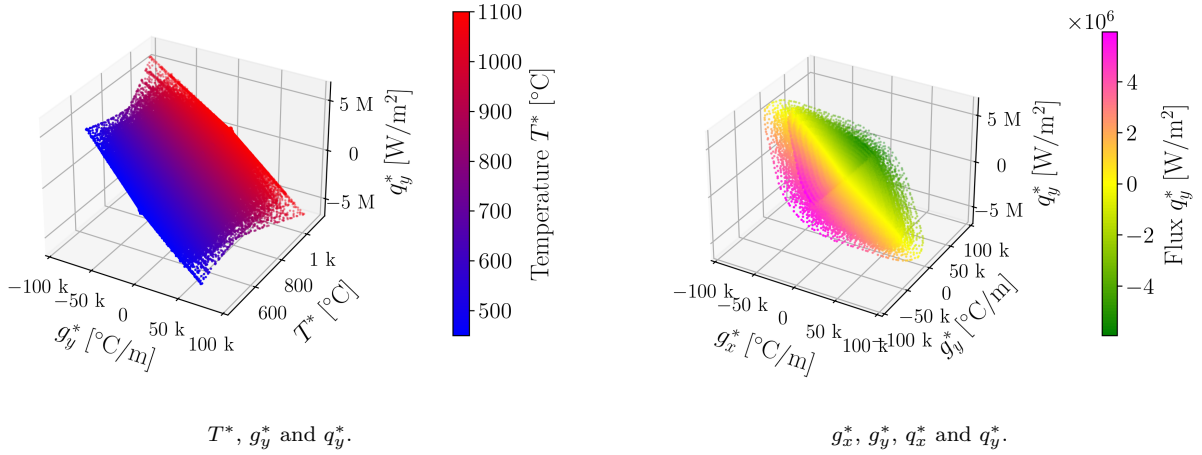


Figure A.3: Material dataset created by synthetic experiments.

To find the closest point  $\{\mathbf{g}^*, \mathbf{q}^*\}_{4D}$  on the line

$$\mathbf{q}^* = -k\mathbf{g}^* \quad (\text{B.1})$$

to the field values  $\{\mathbf{g}, \mathbf{q}\}_{4D}$  at an integration point, the data search can be replaced by the following algorithm. First the distance of the point  $\{\mathbf{g}^*, \mathbf{q}^*\}_{4D}$  to the line (B.1) is defined as:

$$\text{dist}(\{\mathbf{g}, \mathbf{q}\}_{4D}, \mathbf{q}^* + k\mathbf{g}^* = 0) = \frac{|\mathbf{q} + k\mathbf{g}|}{\sqrt{1 + k^2}}. \quad (\text{B.2})$$

Then the closest point on the line to the field values  $\{\mathbf{g}, \mathbf{q}\}_{4D}$  is found by:

$$\begin{aligned} \mathbf{q}^* &= \frac{k(k\mathbf{q} - \mathbf{g})}{1 + k^2} \\ \mathbf{g}^* &= \frac{(-k\mathbf{q} + \mathbf{g})}{1 + k^2}, \end{aligned} \quad (\text{B.3})$$

for a linear constitutive relationship.

## References

- T. Vogel, M. T. van Genuchten, M. Cislerova, Effect of the shape of the soil hydraulic functions near saturation on variably-saturated flow predictions, *Advances in Water Resources* 24 (2000) 133–144. doi:10.1016/S0309-1708(00)00037-3.
- H. Matsuo, The effect of porosity on the thermal conductivity of nuclear graphite, *Journal of Nuclear Materials* 89 (1980) 9–12. doi:10.1016/0022-3115(80)90003-3.
- P. R. Amestoy, I. S. Duff, J.-Y. L'Excellent, J. Koster, Mumps: a general purpose distributed memory sparse solver, in: *International Workshop on Applied Parallel Computing*, Springer, 2000, pp. 121–130.
- A. Farrokhnia, A. P. Jivkov, G. Hall, P. Mummery, Large-scale modeling of damage and failure of nuclear graphite moderated reactor, *Journal of Pressure Vessel Technology* 144 (2022) 031502.
- O. C. Zienkiewicz, R. L. Taylor, *The finite element method*, 5th ed ed., Butterworth-Heinemann, 2000.
- G. D. Smith, *Numerical solution of partial differential equations: finite difference methods*, Oxford university press, 1985.
- H. K. Versteeg, *An introduction to computational fluid dynamics the finite volume method*, 2/E, Pearson Education India, 2007.
- J. T. Katsikadelis, *Boundary elements: theory and applications*, Elsevier, 2002.
- G.-R. Liu, M. B. Liu, *Smoothed particle hydrodynamics: a meshfree particle method*, World scientific, 2003.
- J. P. Boyd, *Chebyshev and Fourier spectral methods*, Courier Corporation, 2001.
- G. S. Gerlero, A. R. Valdez, R. Urteaga, P. A. Kler, Validity of capillary imbibition models in paper-based microfluidic applications, *Transport in Porous Media* 141 (2022) 359–378.
- V. Singh, S. Patra, N. A. Murugan, D.-C. Toncu, A. Tiwari, Recent trends in computational tools and data-driven modeling for advanced materials, *Materials Advances* 3 (2022) 4069–4087.
- A. Tzelepi, P. Ramsay, A. G. Steer, J. Dinsdale-Potter, Measuring the fracture properties of irradiated reactor core graphite, *Journal of Nuclear Materials* 509 (2018) 667–678. doi:10.1016/j.jnucmat.2018.07.024.
- M. S. L. Jordan, P. Ramsay, K. E. Verrall, T. O. van Staveren, M. Brown, B. Davies, A. Tzelepi, M. P. Metcalfe, Determining the electrical and thermal resistivities of radiolytically-oxidised nuclear graphite by small sample characterisation, *Journal of Nuclear Materials* 507 (2018) 68–77. doi:10.1016/j.jnucmat.2018.04.022.
- R. E. Jones, B. L. Boyce, A. L. Frankel, N. Heckman, M. Khalil, J. T. Ostien, F. Rizzi, K. Tachida, G. H. Teichert, J. A. Templeton, *Uncertainty Quantification of Microstructural Material Variability Effects*, Technical Report, Sandia National Lab.(SNL-NM), Albuquerque, NM (United States), 2019.
- M.-H. Edition, N. Bauld, *Mechanics of materials*, PWS Publishers, Boston, Mass. • Belmonte, HMS, Mulheron, MJ, and Smith, PA (2009).“Some observations on the strength and fatigue properties of samples extracted from cast iron water mains.” *Fatigue Fracture Eng. Mater. Struct* 32 (1986) 916–925.
- T. Belytschko, W. K. Liu, B. Moran, K. Elkhodary, *Nonlinear finite elements for continua and structures*, John wiley & sons, 2014.

- M. M. Rao, Foundations of stochastic analysis, Courier Corporation, 2013.
- A. Bensoussan, A model of stochastic differential equation in hubert spaces applicable to navier stokes equation in dimension 2, in: E. Mayer-Wolf, E. Merzbach, A. Shwartz (Eds.), Stochastic Analysis, Academic Press, 1991, pp. 51–73. doi:<https://doi.org/10.1016/B978-0-12-481005-1.50009-0>.
- R. Agarwal, V. Dhar, Big data, data science, and analytics: The opportunity and challenge for is research, 2014.
- B. Baesens, Analytics in a big data world: The essential guide to data science and its applications, John Wiley & Sons, 2014.
- C. M. Bishop, N. M. Nasrabadi, Pattern recognition and machine learning, volume 4, Springer, 2006.
- C. M. Bishop, Neural networks for pattern recognition, Oxford university press, 1995.
- K. Arulkumaran, M. P. Deisenroth, M. Brundage, A. A. Bharath, Deep reinforcement learning: A brief survey, IEEE Signal Processing Magazine 34 (2017) 26–38.
- J. Pateras, P. Rana, P. Ghosh, A taxonomic survey of physics-informed machine learning, Applied Sciences 13 (2023) 6892.
- K. Linka, M. Hillgärtner, K. P. Abdolazizi, R. C. Aydin, M. Itskov, C. J. Cyron, Constitutive artificial neural networks: A fast and general approach to predictive data-driven constitutive modeling by deep learning, Journal of Computational Physics 429 (2021) 110010.
- M. Raissi, P. Perdikaris, G. E. Karniadakis, Physics-informed neural networks: A deep learning framework for solving forward and inverse problems involving nonlinear partial differential equations, Journal of Computational physics 378 (2019) 686–707.
- T. G. Grossmann, U. J. Komorowska, J. Latz, C.-B. Schönlieb, Can physics-informed neural networks beat the finite element method?, 2023. [arXiv:2302.04107](https://arxiv.org/abs/2302.04107).
- T. Kirchdoerfer, M. Ortiz, Data-driven computational mechanics, Computer Methods in Applied Mechanics and Engineering 304 (2016) 81–101. doi:[10.1016/j.cma.2016.02.001](https://doi.org/10.1016/j.cma.2016.02.001).
- T. Kirchdoerfer, M. Ortiz, Data driven computing with noisy material data sets, Computer Methods in Applied Mechanics and Engineering 326 (2017) 622–641. doi:[10.1016/j.cma.2017.07.039](https://doi.org/10.1016/j.cma.2017.07.039).
- J. Ayensa-Jiménez, M. H. Doweidar, J. A. Sanz-Herrera, M. Doblaré, A new reliability-based data-driven approach for noisy experimental data with physical constraints, Computer Methods in Applied Mechanics and Engineering 328 (2018) 752 – 774. doi:<https://doi.org/10.1016/j.cma.2017.08.027>.
- L. T. K. Nguyen, M. Rambausek, M.-A. Keip, Variational framework for distance-minimizing method in data-driven computational mechanics, Computer Methods in Applied Mechanics and Engineering 365 (2020) 112898.
- S. Conti, S. Müller, M. Ortiz, Data-Driven Problems in Elasticity, Archive for Rational Mechanics and Analysis 229 (2018) 79–123. doi:[10.1007/s00205-017-1214-0](https://doi.org/10.1007/s00205-017-1214-0).
- L. T. K. Nguyen, M.-A. Keip, A data-driven approach to nonlinear elasticity, Computers & Structures 194 (2018) 97 – 115. doi:<https://doi.org/10.1016/j.compstruc.2017.07.031>.

- R. Eggersmann, T. Kirchdoerfer, S. Reese, L. Stainier, M. Ortiz, Model-free data-driven inelasticity, *Computer Methods in Applied Mechanics and Engineering* 350 (2019) 81 – 99. doi:<https://doi.org/10.1016/j.cma.2019.02.016>.
- P. Carrara, L. De Lorenzis, L. Stainier, M. Ortiz, Data-driven fracture mechanics, *Computer Methods in Applied Mechanics and Engineering* 372 (2020) 113390. doi:[10.1016/j.cma.2020.113390](https://doi.org/10.1016/j.cma.2020.113390).
- L. Stainier, A. Leygue, M. Ortiz, Model-free data-driven methods in mechanics: material data identification and solvers, *Computational Mechanics* 64 (2019) 381–393. doi:[10.1007/s00466-019-01731-1](https://doi.org/10.1007/s00466-019-01731-1).
- A. Leygue, M. Coret, J. Réthoré, L. Stainier, E. Verron, Data driven constitutive identification (2017).
- A. Leygue, M. Coret, J. Réthoré, L. Stainier, E. Verron, Data-based derivation of material response, *Computer Methods in Applied Mechanics and Engineering* 331 (2018) 184–196.
- G. Valdés-Alonzo, C. Binetruy, B. Eck, A. García-González, A. Leygue, Phase distribution and properties identification of heterogeneous materials: A data-driven approach, *Computer Methods in Applied Mechanics and Engineering* 390 (2022) 114354.
- J. Mora-Macías, J. Ayensa-Jiménez, E. Reina-Romo, M. H. Doweidar, J. Domínguez, M. Doblaré, J. A. Sanz-Herrera, A multiscale data-driven approach for bone tissue biomechanics, *Computer Methods in Applied Mechanics and Engineering* 368 (2020) 113136.
- K. Karapiperis, L. Stainier, M. Ortiz, J. E. Andrade, Data-driven multiscale modeling in mechanics, *Journal of the Mechanics and Physics of Solids* 147 (2021) 104239.
- J. Ayensa-Jiménez, M. H. Doweidar, J. A. Sanz-Herrera, M. Doblaré, An unsupervised data completion method for physically-based data-driven models, *Computer Methods in Applied Mechanics and Engineering* 344 (2019) 120–143.
- T. F. Korzeniowski, Data-driven finite element computation with material uncertainty, PhD Thesis, Universität Siegen, 2022. doi:<http://dx.doi.org/10.25819/ubsi/10181>, backup Publisher: Institut für Mechanik und Regelungstechnik - Mechatronik Publication Title: Schriftenreihe der Arbeitsgruppe für Technische Mechanik im Institut für Mechanik und Regelungstechnik - Mechatronik.
- A. Kuliková, A. G. Shvarts, L. Kaczmarczyk, C. J. Pearce, Data-driven finite element method, 2021. doi:[10.17028/rd.lboro.14588577.v1](https://doi.org/10.17028/rd.lboro.14588577.v1).
- D. Boffi, F. Brezzi, M. Fortin, et al., *Mixed finite element methods and applications*, volume 44, Springer, 2013.
- F. Brezzi, D. Boffi, L. Demkowicz, R. Durán, R. Falk, M. Fortin, *Mixed finite elements, compatibility conditions, and applications*, Springer 2 (2008) 4–2.
- M. F. Wakeni, A. Aggarwal, L. Kaczmarczyk, A. T. McBride, I. Athanasiadis, C. J. Pearce, P. Steinmann, A p-adaptive, implicit-explicit mixed finite element method for diffusion-reaction problems, *International Journal for Numerical Methods in Engineering* 123 (2022) 3237–3263.
- D. N. Arnold, *Mixed finite element methods for elliptic problems*, *Computer methods in applied mechanics and engineering* 82 (1990) 281–300.

- M. Ainsworth, A posteriori error estimation for lowest order raviart–thomas mixed finite elements, *SIAM Journal on Scientific Computing* 30 (2008) 189–204.
- D. Braess, R. Verfürth, A posteriori error estimators for the raviart–thomas element, *SIAM Journal on Numerical Analysis* 33 (1996) 2431–2444.
- C. Carstensen, A posteriori error estimate for the mixed finite element method, *Mathematics of Computation* 66 (1997) 465–476.
- N. Zander, H. Bériot, C. Hoff, P. Kodl, L. Demkowicz, Anisotropic multi-level hp-refinement for quadrilateral and triangular meshes, *Finite Elements in Analysis and Design* 203 (2022) 103700. doi:<https://doi.org/10.1016/j.finel.2021.103700>.
- L. Demkowicz, *Mathematical theory of finite elements*, volume 28.;28;, Society for Industrial and Applied Mathematics, Philadelphia, 2024.
- B. K. Larkin, S. W. Churchill, Heat transfer by radiation through porous insulations, *AIChE Journal* 5 (1959) 467–474. doi:[10.1002/aic.690050413](https://doi.org/10.1002/aic.690050413).
- A. Kulikova, *AdrianaKul / mofem\_data\_driven\_finite\_elements* — Bitbucket, 2021. URL: [https://bitbucket.org/AdrianaKul/mofem\\_data\\_driven\\_finite\\_elements/src/develop/](https://bitbucket.org/AdrianaKul/mofem_data_driven_finite_elements/src/develop/).
- L. Kaczmarczyk, Z. Ullah, K. Lewandowski, X. Meng, X.-Y. Zhou, I. Athanasiadis, H. Nguyen, C.-A. Chalons-Mouriesse, E. Richardson, E. Miur, A. Shvarts, M. Wakeni, C. Pearce, MoFEM: An open source, parallel finite element library, *Journal of Open Source Software* 5 (2020) 1441. doi:[10.21105/joss.01441](https://doi.org/10.21105/joss.01441).
- J. H. Lienhard, IV, J. H. Lienhard, V, *A Heat Transfer Textbook*, 5th ed., Phlogiston Press, Cambridge, MA, 2020. Version 5.10.
- D. McEligot, W. D. Swank, D. L. Cottle, F. I. Valentin, Thermal properties of G-348 graphite, Technical Report, Idaho National Lab.(INL), Idaho Falls, ID (United States), 2016.
- A. Guttman, R-trees: A dynamic index structure for spatial searching, in: *Proceedings of the 1984 ACM SIGMOD international conference on Management of data*, 1984, pp. 47–57.
- R. Eggersmann, L. Stainier, M. Ortiz, S. Reese, Efficient data structures for model-free data-driven computational mechanics, *Computer Methods in Applied Mechanics and Engineering* 382 (2021) 113855.
- B. Bahmani, W. Sun, A kd-tree-accelerated hybrid data-driven/model-based approach for poroelasticity problems with multi-fidelity multi-physics data, *Computer Methods in Applied Mechanics and Engineering* 382 (2021) 113868.
- M. Ainsworth, J. Coyle, Hierarchic finite element bases on unstructured tetrahedral meshes, *International journal for numerical methods in engineering* 58 (2003) 2103–2130.
- A. Kulikova, *Data-driven weaker mixed formulation for diffusion problems*, Ph.D. thesis, 2025. URL: <https://zenodo.org/records/14635488>. doi:[10.5281/zenodo.14635488](https://doi.org/10.5281/zenodo.14635488).
- J. Bonet, R. D. Wood, *Nonlinear continuum mechanics for finite element analysis*, Cambridge university press, 1997.

- J. T. Oden, L. Demkowicz, W. Rachowicz, T. A. Westermann, Toward a universal hp adaptive finite element strategy, part 2. a posteriori error estimation, *Computer methods in applied mechanics and engineering* 77 (1989) 113–180.
- S. Repin, A posteriori estimates for partial differential equations, Walter de Gruyter, 2008.
- T. Grätsch, K.-J. Bathe, A posteriori error estimation techniques in practical finite element analysis, *Computers & structures* 83 (2005) 235–265.
- B. T. Kelly, Graphite—the most fascinating nuclear material, *Carbon* 20 (1982) 3–11.

## List of Symbols

- $\mathbf{g}$  gradient of temperature [ $^{\circ}\text{C}/\text{m}$ ]; a field of temperature gradient.
- $s$  source term [ $\text{W}/\text{m}^3$ ].
- $T$  temperature [ $^{\circ}\text{C}$ ]; a field of temperature.
- $k$  thermal conductivity [ $\text{W}/(\text{m}\cdot^{\circ}\text{C})$ ].
- $h$  element size [ $\text{m}$ ].
- $p$  approximation order for temperature field.
- $t_h$  tolerance for the mesh refinement according to the value of average error estimator.
- $t_p$  tolerance for the order increase according to the value of average error estimator.
- $\xi$  comparative value for data-driven refinement.
- $t_{ave}$  tolerance for the average distances to the material dataset.
- $d_{ave}$  average distance to the material dataset.
- $t_{std}^{ave}$  tolerance for the standard deviation of the distances to the material dataset compared to the average distances in element.
- $t_{std}$  tolerance for the standard deviation of the distances to the material dataset.
- $d_{std}$  standard deviation of the distances to the material dataset.
- $\psi$  perturbation value.
- $\kappa$  standard deviation of the perturbation value.